

POSTPRINT (PEER-REVIEWED, PUBLISHED, JOURNAL-TYPESET COPY)

This manuscript is a **postprint** uploaded to EarthArXiv. It has been peer-reviewed and published in **BASIN RESEARCH** on the **11/09/2020**, and has the DOI **10.1111/bre.12518**. Authors welcome comments, feedback, and discussions anytime.

Feel free to get in contact: geo.david.fernandez@gmail.com

Sedimentation and viscosity controls on forearc high growth

David Fernández-Blanco^{1,2}  | Utsav Mannu³  | Teodoro Cassola⁴ | Giovanni Bertotti⁵ | Sean D. Willett¹

¹Geological Institute, Swiss Federal Institute of Technology (ETH), Zürich, Switzerland

²Barcelona Center of Subsurface Imaging, Institut de Ciències del Mar (ICM-CSIC), Barcelona, Spain

³Department of Earth and Climate Science, IISER Pune, Pune, India

⁴Schlumberger GmbH, Aachen, Germany

⁵Department of Geoscience and Engineering, Faculty of Civil Engineering and Geosciences, Delft, University of Technology, Delft, the Netherlands

Correspondence

David Fernández-Blanco, Geological Institute, Swiss Federal Institute of Technology (ETH), Zürich, Switzerland.
Email: geo.david.fernandez@gmail.com

Funding information

Nederlandse Organisatie voor Wetenschappelijk Onderzoek; Vertical Anatolian Movement Project (VAMP) - Miocene tectonics in the Central Anatolia Plateau

Abstract

Crustal rheology and surface processes strongly influence strain distribution and shape of orogenic wedges at their front but how they influence the wedge rear is still unclear. Here, we analyse the coupled control of viscosity and sedimentation on forearc high growth during advanced stages of subduction accretion. We use 2D thermo-mechanical finite element models constrained with data of the south Anatolian margin. Our simulations show that forearc highs grow as a thermally-activated viscosity drop in the lower crust induces ductile deformation and viscous flow. Initial viscosity and the amount of sediments in the forearc basin control non-linearly the occurrence and timing of the thermally-activated viscosity drop, and thus of the growth of the forearc high. High sedimentation rates result in thicker forearc basins that stabilise the subduction wedge and delay the onset of uplift in the forearc high. Low viscosities promote earlier onset of forearc high uplift and lead to larger morphological variability along the subduction margin. Increasing either the sedimentation rate or viscosity may prevent forearc high formation entirely. The thermo-viscous forearc highs grow at an age set by wedge thermal state as a function of accretionary flux, wedge viscosity, and synorogenic sedimentation. Our models explain vertical motions in south Anatolia and potentially in other accretionary margins, like the Lesser Antilles or Cascadia, during the formation of their broad forearc highs.

KEYWORDS

Central Anatolian Plateau, forearc, forearc basin, orogenic wedge, outer-arc high, Turkey, uplift

1 | INTRODUCTION

Orogenic wedges growing by accretion develop characteristic cross-sectional shapes that result from the balance between basal traction in the subduction thrust and gravity, as modulated by orogenic wedge rheology and internal strain (Davis et al., 1983; Platt, 1986; Willett, 1992). The geometry of the wedge front is controlled by brittle deformation and prescribed by the mechanical properties of the accreting wedge and that of its surface of accretion (Dahlen, 1984;

Davis et al., 1983). The geometry of the wedge rear, however, is less well understood, given its dependence on the non-linear ductile dynamics of the deeper sectors of the wedge (Pavlis & Bruhn, 1983).

Orogen rheology and surface processes markedly influence the first-order evolution of accreting orogenic wedges. Syntectonic erosion (e.g. Koons, 1990; Willett, 1999) and sedimentation (e.g. Erdős et al., 2015; Fillon et al., 2013; Willett & Schlunegger, 2010) affect the distribution of strain and the deformation patterns within the wedge. Higher

ductility results in structures otherwise absent, like backward thrusting sequences (Smit et al., 2003). How these factors and their feedback influence the development and evolution of topography in the wedge internal sectors are difficult to generalise and often overlooked, limiting our understanding of the dynamic interactions amongst surface and deep processes at the orogenic scale.

Forearc systems in accretionary margins have characteristic trench-parallel structures and derived stratigraphies (Dickinson & Seely, 1979) (Figure 1). Forearc highs are plateau-like elevated areas developing in internal regions of some, albeit not all, forearc systems, and their formation may be explained by several mechanisms. Forearc highs may form by upward terrain growth during the forced mechanical accretion of material against areas with higher relative strength commonly referred to as backstops (e.g. Byrne et al., 1993; Kopp & Kukowski, 2003). Under this viewpoint, the strength contrast controls the formation of the forearc high, its structure, and the limits of the wedge (Kopp & Kukowski, 2003). Alternatively, forearc highs may uplift dynamically, supported

Highlights

- 2D FEM analysis of viscosity and sedimentation influence on forearc high growth.
- Forearc highs can grow without backstop at an age set by accretionary flux and wedge thermal state.
- High sedimentation rates lead to thicker forearc basins and later onset of the forearc high uplift.
- Low viscosities lead to larger morphological variability and earlier onset of forearc high uplift.
- Increasing either the sedimentation rate or viscosity may prevent forearc high formation entirely.

by high temperatures and heat production in the deeper sectors of large subduction wedges (e.g. Pavlis & Bruhn, 1983; Vanderhaeghe et al., 2003). In this context, forearc highs may grow by the thermal activation of viscosity in the lower crust, guided by sediment deposition in the forearc basin, and ductile deformation sustained by sediment accretion (Fuller et al., 2006).

In this paper, we focus on this thermo-viscous mechanism of crustal flow and forearc uplift, which has been recently argued to be consistent with the pattern of space-time deformation exhibited by the Cyprus-Anatolia margin (Fernández-Blanco et al., 2020). We elaborate on this model to demonstrate the relationship between sedimentation rates and rheology with temperature, strain patterns, and growth of the accretionary wedge. We analyse how syn-accretion sedimentation in the forearc basin and the viscous state of the subduction wedge control the thermo-viscous uplift of the forearc high. We use 2D thermo-mechanical finite element simulations that include critical wedge visco-plastic mechanics and isostatic compensation, as well as variations in sediment input, rheological behaviour, and thermal conductivity. We build our models to be consistent with the geometry and geologic history of the Central Cyprus accretionary margin. We perform a parametric study focused on how sedimentation rate and specific viscous rheological parameters influence the temperature distribution, strain rate, and localisation in the accretionary wedge internal sectors, and specifically under the forearc high area. For all simulations, we focus on the wavelength and relative age of vertical motions in the upper crust. We find that the dynamic growth of forearc highs can take place non-linearly in time and can explain short-wavelength vertical motions in inland sectors of subduction wedges.

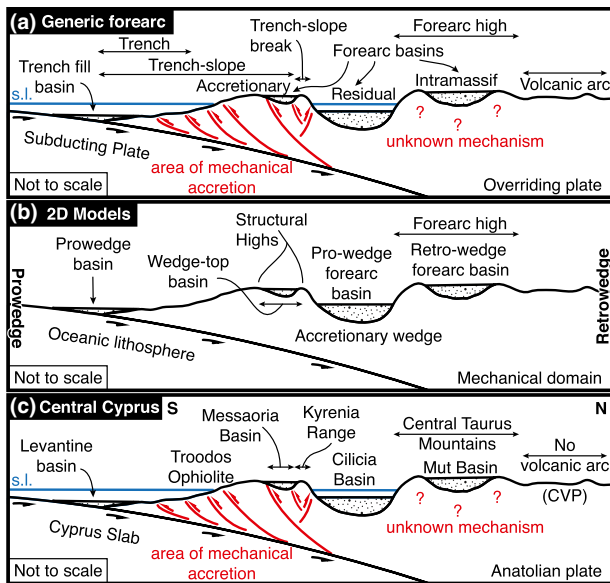


FIGURE 1 Accretionary margins in nature and models. Main morphotectonic features in (a) a generic accretionary margin with forearc high, in (b) models of subduction wedge accretion, and (c) their correlation to features in Central Cyprus. For natural examples, we use original definitions by Karig & Sharman (1975) and Dickinson and Seely (1979), and for numerical models a simpler nomenclature (e.g. Fuller, 1996). ‘Trench-fill basin’ and ‘accretionary forearc basin’ are the nature equivalents to ‘pro-wedge’ and ‘wedge-top’ basins in models, and the terms ‘residual’ and ‘intramassif forearc basins’ of Dickinson and Seely (1979) are in simulations the ‘landward’ and ‘seaward’ forearc basins, respectively. Correlation with elements along the Central Cyprus margin is based in Fernández-Blanco et al. (2020)

2 | FOREARC ELEMENTS OF ACCRETIONARY SUBDUCTION WEDGES

We define morphotectonic features of arc-trench regions for generic accretionary margins in nature and in simulations and relate them to elements along Central Cyprus (Figure 1). In nature, forearcs in accretionary systems exhibit a seaward area under mechanical accretion and an inland area where a forearc basin may be disrupted by a forearc high (Dickinson & Seely, 1979) (Figure 1a). Imbricate seaward-verging thrusts in the seaward sector increase topography landwards from the trench to the trench-slope break, where landward-verging thrusts result in landward-dipping slopes. A trench-fill basin develops above the trench and accretionary basins lay along the trench-slope region as ‘piggy-back’ basins carried atop thrust sheets. Landward, between the trench-slope break and volcanic arc, the forearc high may divide the forearc basin into residual and intramassif basins (Figure 1a).

In models, shear zones develop convex-up ‘structural highs’ enclosing convex-down ‘topographic depressions’. We identify both features with respect to the actively deforming sector of the wedge and by location along the model transect (Figure 1b). In model pro-wedge (seaward), topographic depressions lead to the pro-wedge and wedge-top basins (DeCelles & Giles, 1996). The area of active deformation is limited landward by the structural high, and farther towards the model retro-wedge, the growth of the forearc basin sets a stable area. When present, the forearc structural high defines forearc basins at its front and at its back, named the pro- and retro-wedge forearc basins (Figure 1b). We use negative-alpha basin both in nature and in models to refer to a basin that has a hypothetical critical slope dipping landward and no internal deformation, as it slides above the subduction thrust for as long as it is restricted and steadily infilled to its bounding highs (Fuller et al., 2006; Willett & Schlunegger, 2010).

First-order morphotectonic features in the current arc-trench region of Central Cyprus correlate with the elements described above (Figure 1c). At the southern end of the over-riding Anatolian plate, the northern end of the Levantine Basin may be seen as a trench-fill basin. Northward, the Troodos Ophiolite and the piggy-back Mesaoria wedge-top basin compound the trench-slope, and the Kyrenia Range is the trench-slope break. Farther north, the Cilicia Basin is a residual basin seaward of the Mut Basin, an intramassif basin within the modern Central Taurus forearc high (Figure 1c).

Surface uplift of the forearc high of the Central Cyprus subduction margin spans for an area of ~200 km N-S and ~350 km E-W and led to the modern Central Taurus Mountains of South Turkey (Figure 1). Surface uplift of the modern Central Taurus Mountains occurred since the latest Miocene (post-8Ma) (e.g. Cosentino et al., 2012; Meijers et al., 2018) with no regional fault at the surface (Fernández-Blanco

et al., 2019). The underlying causes behind surface uplift in South Turkey remain debated, with several studies proposing slab break-off (see Schildgen et al., 2014 for a review), and more recent work, suggesting crustal thickening (Meijers et al., 2018) and ductile flow following thermally-activated viscosity in the lower Anatolian crust (Fernández-Blanco et al., 2020). The latter mechanism is consistent with the thick Anatolian crust and lithosphere and the presence of the Cyprus slab under the modern Central Taurus Mountains (e.g. Abgarmi et al., 2017; Bakırcı et al., 2012; Delph et al., 2017), as well as the, coupled, short-wavelength vertical motions reported for South Turkey and its offshore during plateau margin growth (Fernández-Blanco et al., 2019; Walsh-Kennedy et al., 2014).

3 | METHODS: THERMO-MECHANICAL FINITE ELEMENT MODELS

3.1 | Numerical model description

We used 2D thermo-mechanical finite element numerical models that simulate a transect whose specific geometry and parameters are selected to fit the Anatolian margin at the longitude of central Cyprus. Models simulate the thermo-mechanical processes within a deforming forearc, subject to brittle and ductile deformation along with active sedimentation within wedge-top basins. Our models use the numerical formulation described by Fullsack (1995), Pope and Willett (1998), Fuller et al. (2006), Fuller et al. (2006), and include recent modifications for sedimentation, strain softening and healing, and material tracking (Cassola, 2013).

Our models have two nested and coupled domains (Figure 2) that solve for mechanical and thermal processes. The mechanical domain represents the crust of an accreting subduction zone and its internal deformation is calculated dynamically as a response to imposed motions at its boundaries. At the base of the mechanical domain, tangential velocities drive the accretion of incoming sediments. Imposed tangential velocities are coupled with the overlying crust through a frictional slip boundary condition, permitting complete decoupling depending on tangential and normal stresses. The lower boundary has a discontinuity point, S, that represents the contact between the subducting slab and the continental Moho (Figure 2). However, the importance of this boundary is reduced by the frictional slip permitted along the slab interface. The thermal domain spans the mechanical domain and the underlying upper mantle, including the downgoing slab and upper-plate upper mantle. The velocity and geometry of the slab are specified and thus serve as a kinematic component of the model, used for heat advection, but only as a boundary condition for the mechanical deformation. See

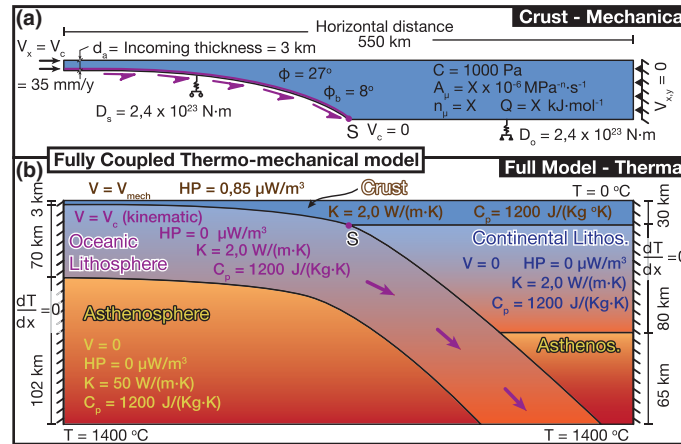


FIGURE 2 Model setup. Model setup, with the specification of thermal and mechanical parameters. S is the point where the subducting plate contacts the Moho of the upper plate. A set of velocities, V , are defined with regards to a fixed frame in the upper-plate interior: V_x and V_y are the components of velocity in horizontal and vertical directions, respectively, and V_{mech} is the 2-D velocity in the mechanical domain and is a free variable. Boundary conditions are a constant convergence velocity, V_c , applied to the left side, and the base of the subducting plate. Boundary between slab and upper plate has a frictional failure criterion, by which relative slip occurs on the boundary once the criterion is exceeded. The incoming sediments have a thickness of d_a . D_s is the flexural rigidity of the subducting plate and D_o is that of the overriding plate. The internal friction angle is shown as ϕ , and the friction angle between plates is ϕ_b . A_μ is the coefficient of the power-law viscosity and n_μ is its coefficient, with Q being the activation energy. HP = heat production, K = thermal conductivity, C_p = specific heat, C = cohesion and T = temperature. Material deforms viscously until yield stress is exceeded, at which point it deforms to satisfy the yield criterion

more detailed information on the thermal computation in the supplementary material. The slab and the lithosphere of the upper plate are permitted to deform by surface loading on the basis of a flexural isostasy model (Fernández-Blanco et al., 2020; Fuller et al., 2006). The mechanical model includes temperature-dependent rheology that sustains brittle/frictional behaviour at low temperatures and a power-law viscous behaviour according to an Arrhenius model relating the tensors of deformation rate, D_{ij} , and stress, σ_{ij} :

$$D_{ij} = A_\mu \sigma_{ij}^{n_\mu} \exp\left(\frac{-Q}{RT}\right) \quad (1)$$

where A_μ and n_μ are constants dependent on the material, Q is the activation energy, R is the molar gas constant, and T is the temperature. Strain resulting from this thermally-activated viscosity is thus neglectable under a certain temperature and is the main constituent of deformation above it. All materials have brittle, pressure-dependent yield stress, following a Coulomb criterion. See the supplementary material for more details on model formulation and relevant subroutines, including thermal computation.

3.2 | Model design and parameterisation

Models simulate 25 My of subduction and accretion along a transect of 550 km (Figure 2) that corresponds to the Central Cyprus margin (Fernández-Blanco et al., 2020). We use a

convergence velocity, $V_c = 35$ mm/year, and a thickness of incoming material at the trench of $d = 3$ km. These two parameters are key to the accretionary flux and thus the growth rate of the accretionary wedge and its final size. Although modern values of these parameters are higher and lower, respectively, these values are good averages for the timeframe of interest. The present V_c of 9.3 ± 0.3 mm/year in Cyprus (Reilinger et al., 2006) is unrepresentative of the last 25 Ma, given that the underthrusting of Eratosthenes Seamount below south Cyprus probably results in a deceleration of the present-day velocity of subduction. Current sedimentary thicknesses between 10 and 15 km, found in the East Mediterranean (e.g. Makris & Stobbe, 1984), are probably the highest ever present over the entire Neogene, given the increasing sediment supply from the Nile River and the narrowing of the Eastern Mediterranean Sea.

In the model pro-wedge (left side), the subducting lithosphere is 50 My old and has a thickness of 70 km kept constant during the simulations. Since the accretion of material from the model pro-wedge thickens the mechanical domain as the models progress, we select an initial thickness of 30 km in the retro-wedge of the mechanical domain which, given our chosen accretionary flux, results in a final thickness at the end of the model comparable to observed thicknesses (Figure 3), that is, maximum values of 45 km near the ‘S’ point. We chose a thickness of 80 km for the rest of the overriding lithosphere. The geometry of the slab is curved, from the horizontal to a final dip angle set at the base of the continental lithosphere. We chose this dip in models to be 40°

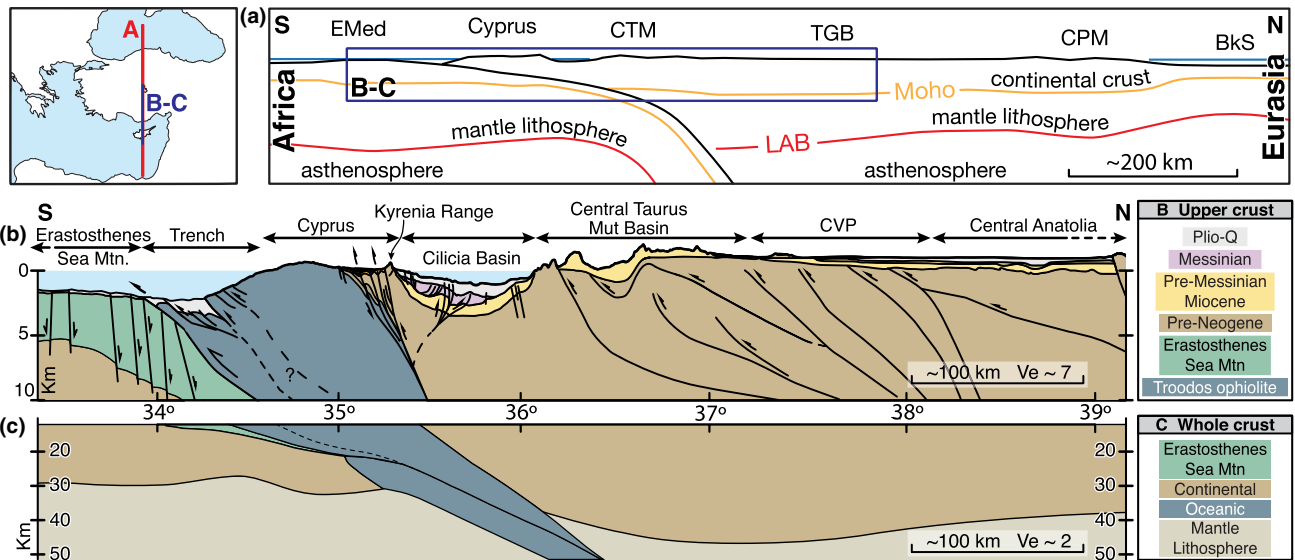


FIGURE 3 Transects along the Anatolian margin in Central Cyprus. Upper-crustal and crustal-scale geological transects running N-S (650 km at around 33°30' E). The transects stretch from the Levantine Basin to the Tuz Gölü Basin across the Cyprus arc-trench, the island of Cyprus, the Cilicia Basin, the Central Taurus Mountains, and the Central Anatolian interior. The upper-left panel is a location map. Panel a is a transect across Central Cyprus and Anatolia, simplified from Stephenson et al. (2004), that has a topo-bathymetry with three times vertical exaggeration. EMed = East Mediterranean; CTM = Central Taurus Mountains; TGB = Tuz Gölü Basin; CPM = Central Pontides Mountains; BkS = Black Sea. Panel b is the upper sector of the transect (up to 10 km depth), shown with a vertical exaggeration of 7, and Panel c is the crustal cross-section for the area. These transects integrate upper crustal studies (Calon et al., 2005a, 2005b; Çiner et al., 2008; Fernández-Blanco et al., 2013; McCay, 2010; Robertson, 1998; Stephenson et al., 2004) with the interpretation of several geophysical studies (Ates et al., 1999; Mart & Ryan, 2002; Abgarmi et al., 2017; Delph et al., 2017; Ergün et al., 2005; Koulakov & Sobolev, 2006; Mutlu & Karabulut, 2011; Özeren & Holt, 2010), as detailed in Fernández-Blanco (2014). CVP = Central Volcanic Province

(based on the 45° reported in Fernández-Blanco et al., 2020), to obtain model slab dips of ~20° at the contact between the slab and the continental Moho.

Flexural rigidity is set at 2.4×10^{23} N-m for both plates, but variations of flexural rigidity values of up to four orders of magnitude do not produce substantial changes. The density of the crust is 2.8 g/cc, and is an average value that includes continental and oceanic crusts, and sedimentary cover. For the mantle and an overlying layer of water, arbitrarily chosen to be 7 km, we use densities of 3.3 g/cc and 1.03 g/cc, respectively. Cohesion is set at $c = 1,000$ Pa primarily to assure stability of steep slopes of near-surface sediments (<3 km), and the parameter has little influence at deeper levels of the crust, given the dominance of the frictional term. An internal friction angle $\varphi = 27^\circ$ in the crust, and a friction angle $\varphi_b = 8^\circ$ at the contact between overriding and subducting plates are low in order to include fluid pressure effects that are not accounted for explicitly, thus implying fluid pressure ratios within valid ranges at accretionary wedges (Fuller, 2006, and the references therein).

3.3 | Model strategy

Our models simulate a transect along any accretionary margin that runs orthogonal to the main transport direction of

the incoming material, where contractional structures develop. Although valid for accretionary subduction wedges elsewhere, we chose a model geometry and history that is comparable to the Anatolian subduction margin in Central Cyprus. We construct a Base Model in which the main parameters are the preferred values for the S-N transect along the Central Cyprus subduction (see Figure 3). Subsequent models are presented as perturbations about this Base Model. Simulations are constrained by the present-day thickness and geometry of sedimentary units, and geological and plate-scale observations at the end of the simulation. However, off-section sources of material in the Anatolian margin, such as the mountainous areas to the north and northeast, and other potentially important three-dimensional effects that might occur in the area are not taken into account.

Our Base Model for Central Cyprus best represents the time evolution of crustal vertical motions since the Early Miocene along the transect. To select our Base Model, we attended to the overall agreement of large-scale structure evolution and vertical motions through time, as well as final geometry, with particular attention to the uplifted region and domains to the south and north of it. Based on our Base Model, the values of maximum sedimentation rate and viscosity for the parameter space have been selected through a model calibration procedure. We subsequently estimate the sensitivity of the model to changes in each parameter, which

are presented as a set of model suites. In the Sedimentation Rate Suite, we study the effect of the selected value of the maximum sedimentation rate. In the Viscosity Suite, we study the rheological parameters of activation energy, Q , the power-law viscosity pre-exponential, A_μ , and the power-law exponent, n_μ , by systematically varying their values.

4 | RESULTS

4.1 | Regional transect from the Mediterranean to Anatolia

We integrated tectono-sedimentary studies with our own data, and interpreted geophysical data from on- and offshore studies synthesised into crustal transects at 33°30' E (Figure 3). Transect A in Figure 3 spans from the African continental shelf to the Black Sea, and is a simplification of the lithospheric-scale transect shown in Stephenson et al., (2004). Crustal and upper-crustal cross-sections in panels b and c offer two original views of transects in Fernández-Blanco et al. (2020), which integrate and interpret geophysical studies in the area of interest.

To constrain the crustal geometries, we reconstruct sections at the upper-crustal and full-crustal scale that span from the Eratosthenes Seamount, in the East Mediterranean Sea, to the interior basins of Central Anatolia. We use a collective interpretation of available geophysical data (e.g. Ergün et al., 2005; Koulakov & Sobolev, 2006; Mutlu & Karabulut, 2011; Özeren & Holt, 2010) along a transect, which is integrated with the TransMed transect VII (Stephenson et al., 2004), and accounts for tomographic constraints from Bakırcı et al. (2012) and Biryol et al. (2011). We reproduce the tectonostratigraphy of Miocene and younger rocks and upper-crustal structures along the transect (Figure 3b,c) integrating own findings (Fernández-Blanco, 2014; Fernández-Blanco et al., 2013, 2019) with regional studies (Calon et al., 2005a, 2005b; Çiner et al., 2008; Harrison et al., 2004; McCay & Robertson, 2013; Robertson, 1998a, 1998b; Stephenson et al., 2004). We assembled the interpretation of these areas as shown in the original studies, and interested readers can find details there.

This integrative effort, which expands and is complementary to that presented in Fernández-Blanco et al. (2020), allows us to constrain four key features; (a) the shape of the subducting slab and the geometry of its contact with the continental crust; (b) the overall distribution of crustal thicknesses; (c) the relative age and cutting relationships of main structures, and; (d) the position, continuity, and geometry of Miocene rocks.

The African plate, composed of the Eratosthenes continental fragment and surrounding oceanic crust, subducts northwards below the thickened continental crust in the south

Anatolian margin. The Cyprus slab reaches an angle of ~20° at the contact with the Anatolian Moho (Figure 3c), and ~45° near the contact with the base of the Anatolian lithosphere (Fernández-Blanco et al., 2020) (Figure 3a). The overriding Anatolian lithosphere varies from ~110 km where its base contacts the slab, to ~85 km at the northern tip of the transect.

Crustal thicknesses vary along the transect (Figure 3c). In the African plate and in the southern end of the transect, changes in crustal thickness can be inferred from gravimetric anomalies (Ergün et al., 2005) and models of the Moho depth (Koulakov & Sobolev, 2006). Crustal thicknesses have average values of ~28 km below the Eratosthenes Seamount and are minimum (~25 km) below the trench. Geophysical models show an increase in Moho depth northward, from ~28 km at 34°30'N to >40 km at 37° N, that we relate with slab steepening. The slab dips 20° at the contact with the continental Moho and maintains a similar dip until 36°30' N, where it steepens (see Figure 2 in Fernández-Blanco et al., 2020). Maximum overriding crustal thicknesses of ~45 km at the point of contact between the African slab and the Anatolian Moho, below the Central Taurus Mountains, suggest crustal thickening in relation to subduction. We use the interpretation of Pn tomography inferring a decrease in crustal thickness to ~35 km in the Central Anatolian interior (Mutlu & Karabulut, 2011) over gravity data (Özeren & Holt, 2010) suggesting a crust up to ~10 km thicker.

South-verging thrusts divide the area along the transect into present-day sedimentary basins and structural highs (Figure 3b). The thrusts become older when progressing northward along the section, and have been linked with the Cyprian subduction megathrust, directly in the south (e.g. Calon et al., 2005a, 2005b; Stephenson et al., 2004) and indirectly in the north (Fernández-Blanco et al., 2019). Thrusts are active at the trench (e.g. Stephenson et al., 2004), Pliocene or younger in North Cyprus (e.g. McCay, 2010), mid-Pliocene in the Cilicia Basin (Aksu et al., 2005), and pre-Miocene in the Mut Basin (e.g. Çiner et al., 2008). Pliocene contractional structures are seen in the Cilicia Basin, but no evidence of any Miocene or younger thrust system is known for the Mut Basin or for the transition between both basins. This transition is marked instead by monoclinial flexure along a kink-band fold that accommodates ~4 km of relative vertical displacement between coeval Miocene rocks with minimum shortening (<1%) (Fernández-Blanco et al., 2019). The aforementioned evidence is compatible with tectonic forcing from the south and northward dissipation of strain across the subduction margin.

From south to north, Miocene rocks outcrop in four different localities: the Mesaoria Basin in Cyprus, the offshore Cilicia Basin, the Mut Basin on the Central Taurus Mountains, and the Tuz Gölü Basin, in the plateau interior (Figure 3b). Basin terminations in all four Miocene basins are erosive and controlled by post-depositional tectonic contacts,

TABLE 1 Main model parameters. Values of the main parameters used for the Base Model, their associated references, and comments on the value choice

Parameter	Description	Value	References	Comment
Base Model for Central Cyprus				
Mechanical Model				
ρ_c	Crust density	2,800 kg/m ³	(Christensen & Mooney, 1995; Dzierwowski & Anderson, 1981)	Generic crustal material composed of oceanic (3,000 kg/m ³) and continental crust (2,700 kg/m ³) and sediments between 1,700 kg/m ³ to 2,650 kg/m ³
ρ_m	Mantle density	3,300 kg/m ³	(Dzierwowski & Anderson, 1981)	Includes the lithospheric mantle and asthenosphere
ρ_w	Water density	1,030 kg/m ³	(e.g., Nayyar et al., 2016)	Seawater
ϕ	Internal friction angle	27°	(e.g., Davis et al., 1983; Flemings & Saffer, 2018)	
ϕ_b	Friction angle between subducting and overriding plate	8°		
c	Cohesion	1,000 Pa	(e.g., Ikari & Kopf, 2011)	Should be between 1–10 MPa. Value used to sustain slope stability in sediments and avoid unrealistic failures affecting model stability. Value not affecting deeper sectors dominated by the friction component
D	Flexural rigidity	$2.4 \times 10^{23} \text{ N} \times \text{m}$	(Ranalli, 1995)	
S_α	Slab angle at S point	40°	(Fernández-Blanco et al., 2020)	Measured at the S point
v_c	Convergence velocity	35 mm/year	$9.3 \pm 0.3 \text{ mm/year}$ in Cyprus (Reilinger et al., 2006)	Unrepresentative for 25 My. See explanation in the main text
h	Sediment thickness in the subducting plate	3 km	Current thicknesses in East Mediterranean of 10–15 km (e.g., Makris & Stobbe, 1984)	Unrepresentative for 25 My. See explanation in the main text
Sed_r	Sedimentation rate	0.5 mm/year		See explanation in the main text
Thermal Model				
H_{sl}	Thickness of the subducting mantle lithosphere	70 km	(e.g., Pasyanos, 2010)	Commonly, 40–130 km
H_{ol}	Thickness of the overriding mantle lithosphere	80 km	(e.g., Pasyanos, 2010)	Commonly, 0–240 km
Ma_{lith}	Age of the subducting lithosphere	50 Ma	Debated	Assumed
t_{runup}	Thermal model run-up	20 My	(Robertson, 1998)	Retreat of the slab near to its present position at 25 Ma

(Continues)

TABLE 1 (Continued)

Base Model for Central Cyprus	
Parameter	Description
$K_{l,a}$	Thermal conductivity (lithosphere, asthenosphere)
T_s	Surface temperature
T_a	Asthenosphere temperature
HP	Heat production
c	Specific heat
A_μ	Power-law viscosity coefficient
n_μ	Power-law viscosity exponent
Q	Activation energy

Value	References
2.0, 50.0 W/(m × °K)	(Ranalli, 1995)
27°C	(Hofmeister, 1999)
1,400°C	(Jaupart & Mareschal, 2005)
0.85 μW/m ³	(Turcotte & Schubert, 2002)
1,200 J/Kg × °K	(Fernandez-Blanco et al., 2020; Ranalli, 1995)
6.46 × 10 ⁻⁶ MPa ⁻ⁿ /s	
2.65	
170 kJ/mol	

Comment
On the same order of magnitude
See also Figure 4
See also Figure 4
See also Figure 4

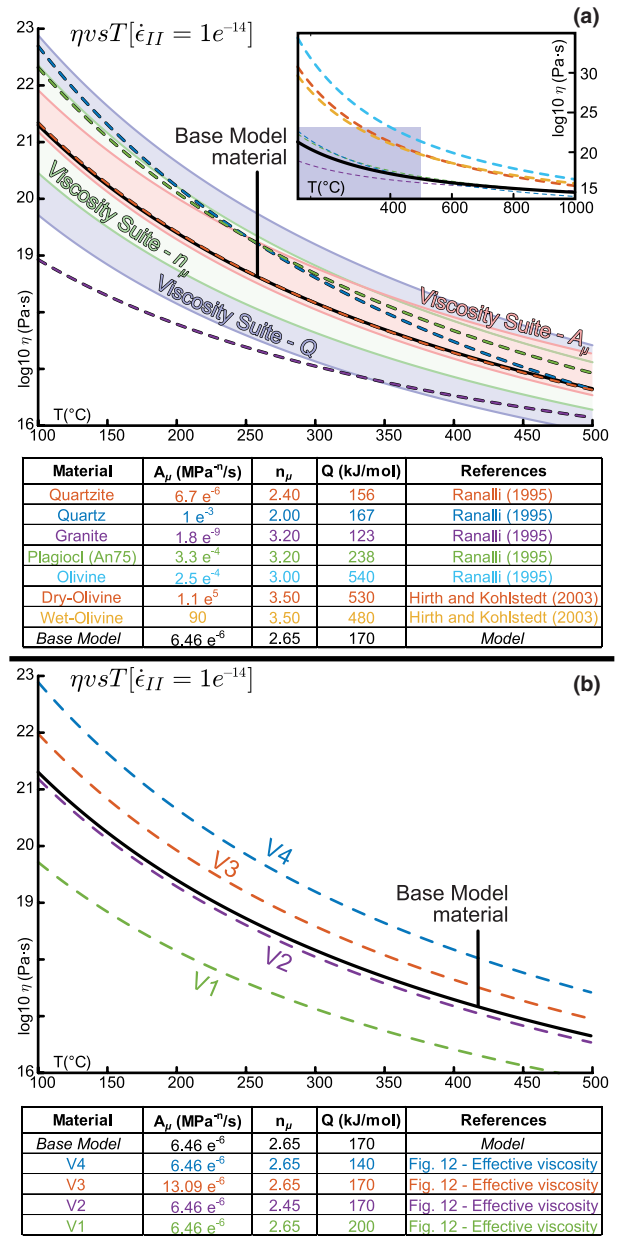


FIGURE 4 Flow-law behaviour of natural and simulated materials. Plot of effective viscosity versus temperature for natural and modelled materials under a constant strain rate ($\epsilon = 10^{-14}$). Panel a shows the flow law behaviour of olivine (+wet, +dry), in the upper right panel, as well as granite, quartz, plagioclase (An75), and quartzite (purple, blue, green, and orange, respectively, in the main panel) alongside that of our Base Model material (black in both panels), and the ranges of parameter values in the viscous suites, which are shown in orange (for A_μ), in green (for n_μ) and in lilac (for Q) in the main panel. The table at the bottom shows the values and studies used. Panel b shows the flow law behaviour of the models shown in Figure 12; V1 (green); V2 (purple); V3 (orange); V4 (blue) and the Base Model material in black

with the exception of the southern margin of the Mesoria Basin, where these rocks pinch out. The middle and upper Miocene sequences infilling these basins are composed

mostly of shallow-water limestones and thus allow for a first-order estimation of vertical kinematics relative to sea level since the end of the Miocene. Rocks above pre-Miocene substratum in the asymmetrical Mesoria Basin thin southward and are disrupted to the north by the imbricate thrusts verging south that uplift the Kyrenia Range (Calon et al., 2005a, 2005b; McCay, 2010). In contrast, the transition between rocks at ~ 2 km in the Cilicia Basin and at ~ 2 km in the Mut Basin is a broad monocline that occurs in the absence of surface-reaching faults (Fernández-Blanco et al., 2019). North of the Mut Basin, Miocene rocks in Central Anatolia are at relatively lower elevations (< 1 km).

4.2 | Base Model for Central Cyprus

Our Base Model uses a maximum sedimentation rate of 0.5 mm/year and viscous parameters values of $Q = 170$ kJ/mol, $A_\mu = 6.46 \times 10^{-6}$ MPa $^{-n}$ /s, and $n_\mu = 2.65$. The complete list of parameter values used in our Base Model is shown in Table 1. Under a given strain rate, the crustal material of our Basic Model yields viscosities similar to those of quartzite, over a wide range of temperatures (see Figure 4).

The time evolution of the mechanical domain of the Base Model is shown in Figure 5 and the correlation amongst temperature, viscosity, and deformation in the area where the

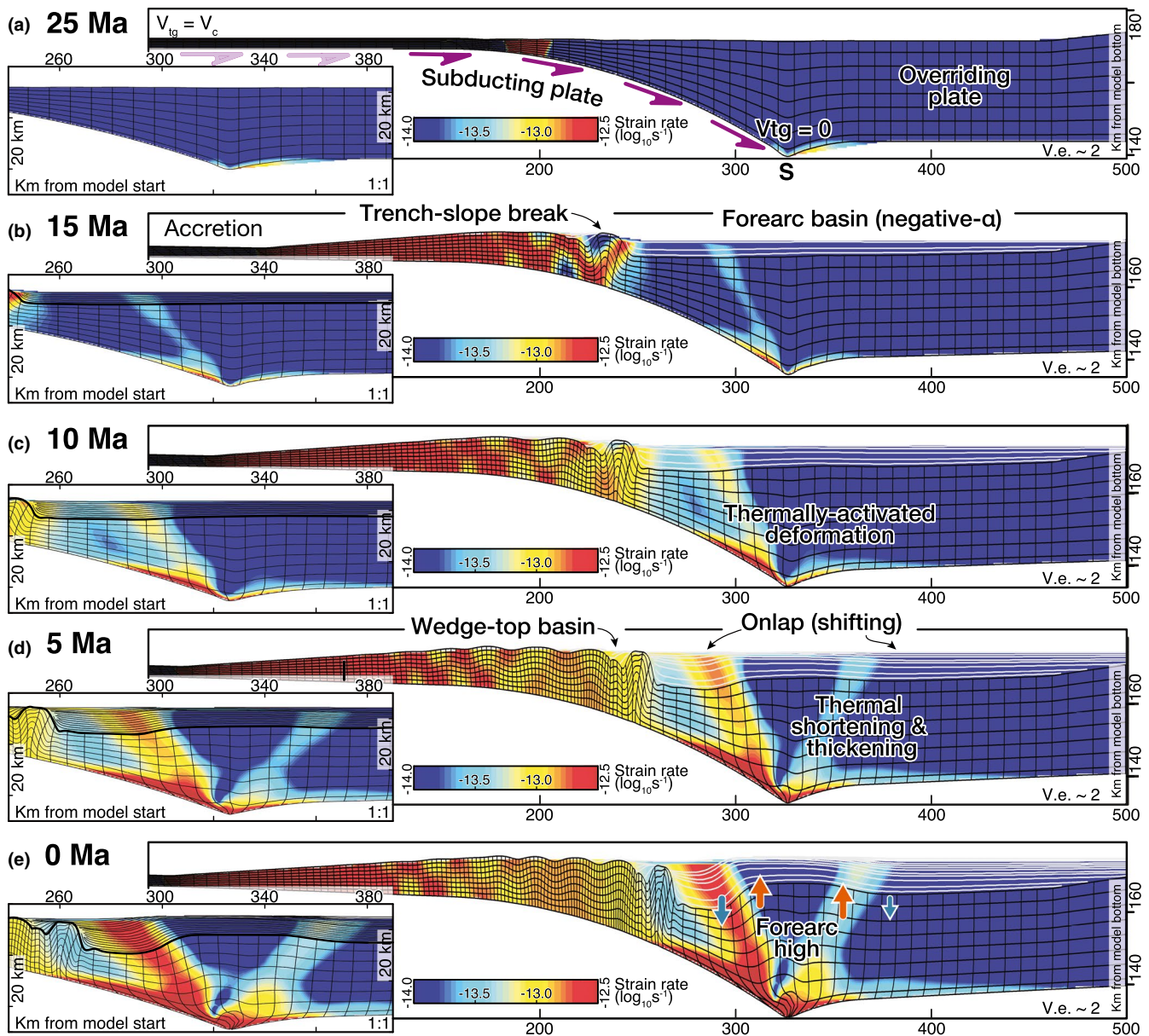


FIGURE 5 Base Model. Mechanical model evolution in time steps, with zoom-ins into the area where the forearc high develops. Times represented are, from top to bottom: 25 Ma, 15 Ma, 10 Ma, 5 Ma, and present. Strain rate is shown in vivid colours ranging from blue (low; $-14.0 \log_{10} s^{-1}$) to red (high; $-12.5 \log_{10} s^{-1}$). The mesh of black lines records cumulative deformation in the basement since model onset. The individual lines on top of the basement (white in main panels and black in zoom-in views) represent isochrones of deposited and subsequently deformed sediment

forearc high develops is shown in Figure 6. The geometry of the mechanical domain at the moment of model initiation (25 Ma) has a roughly flat topography (Figure 5a). In the model retro-wedge (right of the figure), we set a topographic barrier to confine the deposition of sediments within the model and avoid model instability. The curved geometry below the mechanical domain at the model pro-wedge (left of the figure) is set by the down-going slab, which is not shown in the figure. Overall, the temperature is low and viscosity is high along the entire mechanical domain (top panel in Figure 6).

At 10 My after model onset, a large forearc (negative-alpha) basin has developed (Figure 5b). Horizontal isochrones cover the centre and retro-wedge of the model. Topography has started to develop in the model pro-wedge in relation to two shear zones, marked by warmer colours in the second invariant of the strain rate. A small asymmetric wedge-top basin develops between the shear zones that are translated towards the retro-wedge (towards the right) as the shear zones migrate. The subducting slab becomes steeper, while the base of the crust becomes more horizontal. Both factors influence the extent of strain around the 'S' point, at the base of the wedge.

After 15 Ma in model time, further deepening and thickening in the forearc basin leads to increasing strain accumulation,

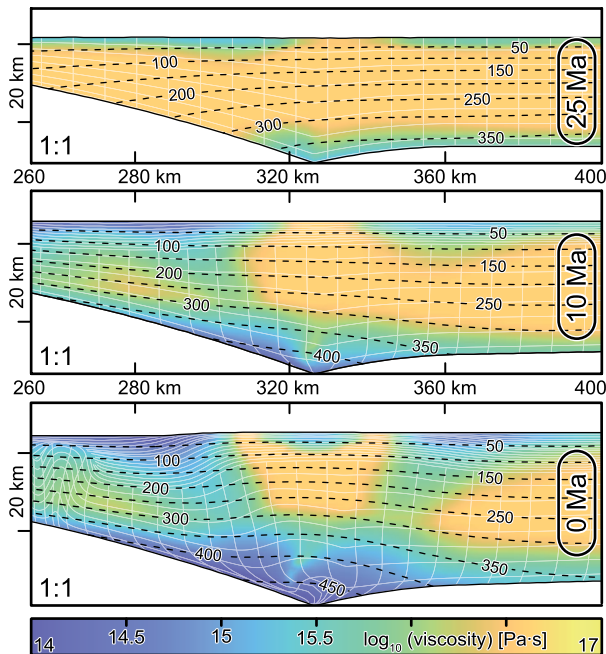


FIGURE 6 Temperature, viscosity, and deformation during forearc high growth. Correlation amongst temperature (in °C, shown as black dashed lines), viscosity (in Pa·s, shown as gradient colours between blue -low- and yellow -high-), and the deformation mesh of the mechanical model (as a grid for the basement and originally-horizontal isochrones for the sedimentary cover, both in light white) in the area where the forearc high develops in three-time steps: 25 Ma, 10 Ma, and present

and temperatures, at the base of the crust (Figure 5c). As the sediments accumulate in the forearc alpha-basin, the initial development of a frontal branch of a shear zone rooted at the 'S' point leads the basement-basin contact to dip towards the model pro-wedge. As the model progresses, the wedge-top basin migrates towards the retro-wedge and the shear zones become wider and more pronounced. Another wedge-top basin starts to develop in the model pro-wedge. The temperature has increased in the frontal and deepest sectors of the mechanical domain thereby decreasing viscosity (middle panel in Figure 6).

At 20 Ma, two shear zones branch out from the 'S' point and produce a broad uplifting bulge above it, in the central-right area of the model (Figure 5d). The shear zones delimit the uplifted area of the forearc high, which dips gently towards the left side of the model. The basement further tilts pro-wedge ward (left), and isochrones mark the onset and development of a monoclinial fold. Overall, horizontal isochrones on top of the bulge transition to isochrones dipping away from the bulge to its sides creating a broad anticlinorium. Onlap relationships take place on both sides of the bulge with larger angles in the model pro-wedge.

At the end of the model run, during the last 5 Ma, vertical motions in the forearc are prominent (Figure 5e). The bulge divided the forearc basin in two, a pro- and a retro-wedge sub-basin, sea- and land-wards, respectively, and onlap relationships to its sides develop further. The deflection of the slab proceeds towards higher angles (~40°) at the 'S' point and the base of the wedge has smaller angles farther towards the retro-wedge. The basement of the pro-forearc basin deepens, while uplift continues in the forearc high. An area with low values in the second invariant of strain rate develops in the uppermost ~5 km of the forearc high. Maximum temperatures and minimum viscosities occur in the deepest sectors of the mechanical domain, while viscosity minima set the shear zones regions in shallower sectors (bottom panel in Figure 6).

4.3 | Sedimentation Rate Model Suite

Sedimentation in the models is 'fill-to-spill' and areas between structural highs that are capable of accommodating sediments are filled to capacity. In doing this, we assume the availability of sufficient sediment throughout the model run. We set each model with a different maximum sedimentation rate that remains constant throughout the model run (Tables 1 and 2, and Figure 7).

Models show that as the maximum sedimentation rate increases, the strain becomes greater in and around the 'S' point and is distributed in shear zones to its sides. The subducting lithosphere becomes steeper towards the model retro-wedge, while the base of the crust further deflects towards the 'S' point. This is, increasing sedimentation leads to an 'S'

TABLE 2 Models and parameterisation. Models used in this study, the values of the four parameters that are changed systematically for the maximum sedimentation rate and viscosity suites, with reference to figures and videos of some representative simulations

Model Run name	Sedimentation rate (mm/year)	Power-law viscosity		Activation energy Q (kJ/mol)	Video in Figures or suppl. material?
		A_μ ($\times 10^{-6}$ MPa $^{-n}$ /s)	n_μ		
Base Model	0.5	6.46	2.65	170	Figures 4–10 and 12
Sedimentation Rate Suite (constant per model)					
Sr0	0.0	6.46	2.65	170	Figure 12 & Video Sr0
Sr1	0.1	6.46	2.65	170	Figure 7
Sr2	0.2	6.46	2.65	170	Video Sr2
Sr3	0.3	6.46	2.65	170	Figure 12
Sr4	0.4	6.46	2.65	170	Video Sr4
Sr5	0.5	6.46	2.65	170	Base Model
Sr6	0.6	6.46	2.65	170	Video Sr6
Sr7	0.7	6.46	2.65	170	Figure 12
Sr8	0.8	6.46	2.65	170	Video Sr8
Sr9	0.9	6.46	2.65	170	Figure 7
Sr10	1	6.46	2.65	170	Figure 12 & Video Sr10
Sr11	1.1	6.46	2.65	170	
Sr12	1.2	6.46	2.65	170	Video Sr12
Sr13	1.3	6.46	2.65	170	
Viscosity Suite (values at model onset)					
A1	0.5	0.15	2.65	170	
A2	0.5	2.37	2.65	170	Figure 8 & Video A2
A3	0.5	4.26	2.65	170	
A4	0.5	6.46	2.65	170	Base Model
A5	0.5	8.27	2.65	170	
A6	0.5	10.88	2.65	170	Figure 8 & Video A6
A7	0.5	13.09	2.65	170	V3 in Figures 4 and 12
n1	0.5	6.46	2.35	170	
n2	0.5	6.46	2.45	170	Figure 9 and Video N2
n3	0.5	6.46	2.55	170	V2 in Figures 4 and 12
n4	0.5	6.46	2.65	170	Base Model

(Continues)

TABLE 2 (Continued)

Model Run name	Sedimentation rate (mm/year)	Power-law viscosity		Activation energy Q (kJ/mol)	Video in Figures or suppl. material?
		$A_\mu (\times 10^{-6} \text{ MPa}^{-n}/\text{s})$	n_μ		
Base Model	0.5	6.46	2.65	170	Figures 4–10 and 12
n5	0.5	6.46	2.75	170	
n6	0.5	6.46	2.85	170	Figure 9 & Video N6
n7	0.5	6.46	2.95	170	
Q1	0.5	6.46	2.65	140	V4 in Figures 4 and 12
Q2	0.5	6.46	2.65	150	Figure 10 & Video Q2
Q3	0.5	6.46	2.65	160	
Q4	0.5	6.46	2.65	170	Base Model
Q5	0.5	6.46	2.65	180	
Q6	0.5	6.46	2.65	190	Figure 10 & Video Q6
Q7	0.5	6.46	2.65	200	V1 in Figures 4 and 12

point that subsides relative to the geoid. However, whereas models with more sediment in the system show a decreasing surface uplift, models with a higher maximum sedimentation rate that surpasses a threshold, exhibit larger surface uplift (see videos Sr0–Sr12 in supplementary materials).

As sedimentation increases, thicker forearc basins develop that tend to stabilise the margin and translate deformation towards the basin margins. This leads to limited forearc uplift (Figure 7, right). The uplifted region above the thermally-activated viscosity becomes broader, and the points of maximum uplift and maximum deposition move landward (see videos Sr8 and Sr10 in supplementary materials). Similarly, vertical displacements are smaller. This effect is recorded as angular discordances in the basin chronolines, showing onlap relationships in models with faster forearc high growth. Increasing sedimentation also results in relative vertical displacements between subsided and uplifted areas that are consistently larger and occur in narrower (horizontally shorter) distances, that is, larger amplitudes in the main subsidence-uplift pair (forearc high - pro-basin).

With low maximum sedimentation rates (Figure 7, left), the initial forearc basin is thin and imposes no restrictions to forearc high surface uplift, which occurs earlier with respect to model onset, that is, forearc high is older, and both downward/upward vertical motions take place over shorter periods (see videos Sr2 and Sr4 in supplementary materials). In general, with lower sedimentation rates the margin is more susceptible to the influence of the other parameters; for example, the incoming sediment at the trench markedly affects the structural evolution of the margin, which exhibits sharper shear zones that migrate towards the retro-wedge of the model faster and structural highs and lows that are larger in amplitude.

4.4 | Viscosity Model Suite

The combination of parameters in Equation (1) determines the effective viscosity of a thermally-activated viscous material, defined as the proportionality constant between strain rate (D_{ij}) and stress (σ_{ij}). With a non-linear stress dependence, the relationship is complicated, but for a given stress level, the effective viscosity determines whether or not the material will flow at a significant rate (see Figure 4) over the geologic timescale of interest. By changing these parameters, we can investigate how changes in the effective viscosity affect deformation in the deep wedge. As a general principle, any decrease in the effective viscosity encourages the flow of the deep crust, and under horizontal compression, leads to crustal thickening and forearc uplift. Table 2 and Figure 4 show the range of values explored.

The pre-exponential viscosity parameter A_μ directly scales the effective viscosity and thereby becomes an explicit control of forearc deformation. Within the parameter

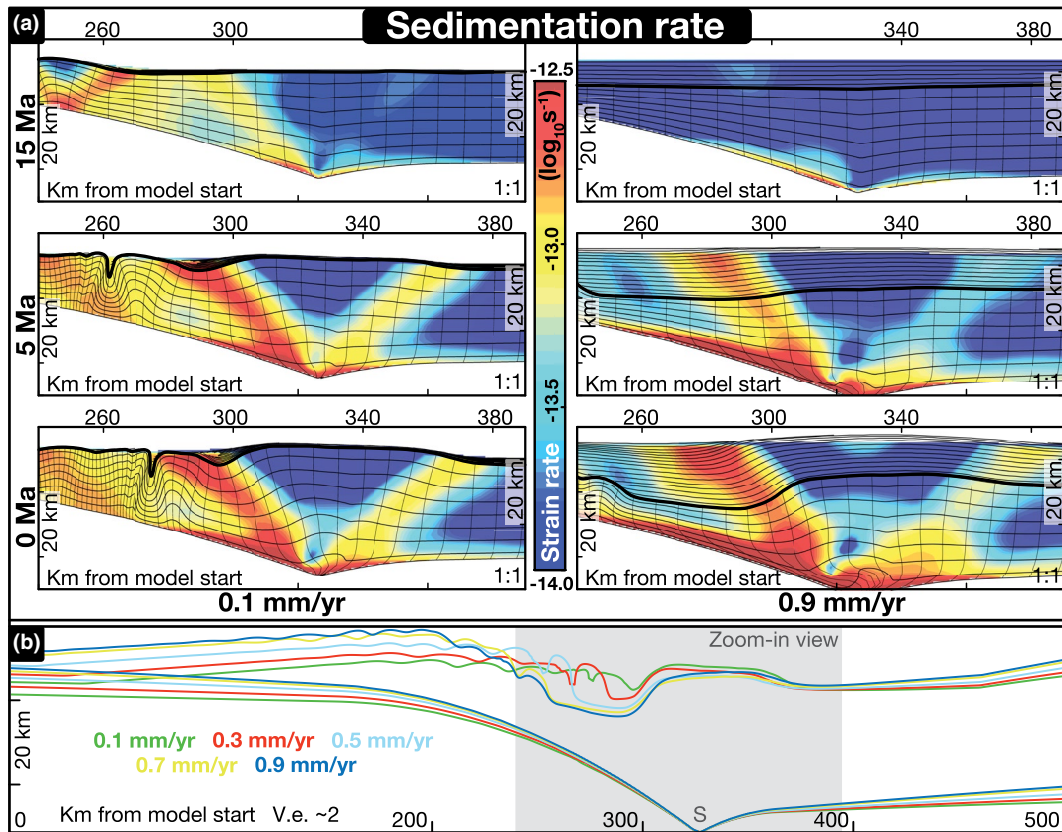


FIGURE 7 Variations in maximum sedimentation rates. Forearc high development with changes in the maximum sedimentation rate. (a) Insets of the forearc high area for models with maximum sedimentation rates of 0.1 mm/year (left column) and 0.9 mm/year (right column) at 15 Ma (top row), 5 Ma (middle row), and 0 Ma (bottom row). The individual black lines on top of the basement represent isochrones that reflect deformation since their successive inception in time, and thus the overall geometric relationships expected for strata. A thicker black line marks the basement-infill contact. (b) Line trace of the bottom of the crust and top of the basement in models with changes in sedimentation rates after a complete run. Vertical reference frame is taken from the 'S' point at the base of the crust. The dimmed grey box shows the approximate location of the zoom-in view in panel a. Upper panels are at 1:1 scale and the bottom panel is at 1:2 scale

range investigated (Table 2; Figure 4), lower values produce a deeper initial forearc basin, but delays the time of formation of the forearc high with respect to our Base Model. A_{μ} affects the amount of relative differential motion between the subsiding and the uplifting sectors of the forearc high and the age of the motions. Forearc high growth cannot counteract the primary subsidence signal (Figure 8, left). Subsidence in the initial forearc basin decelerates with time until the formation of the structural high leads to accelerating subsidence in the pro-basin and protracted decelerating subsidence in the retro-basin (see video A2 in supplementary materials). Higher values of A_{μ} result in the rise of pronounced forearc high that develop in relation to broader shear zones, that is, more diffuse strain, and at earlier times than our Base Model. Forearc high formation outpaces the primary subsidence signal imposed by sediment loading and surface uplift in the forearc high area is eventually larger than the subsidence recorded since forearc basin onset (Figure 8, right). The rate of the motions after forearc high development accelerates with time in both forearc high and pro-forearc basin, resulting

in differential motions that become larger with time in the forearc high pro-wedge, in contrast to its retro-wedge, where the rate of subsidence remains roughly constant (Figure 8; video A6 in supplementary materials).

The parameter n_{μ} exerts control on the age, wavelength, and rate of the relative differential motions in the forearc high area, as it does on strain localisation. Changes in n_{μ} result in a different average viscosity, so the behaviour is similar to A_{μ} , but it also has effects through the greater strain localisation that occurs with a higher exponent. Lower values of n_{μ} within the parameter spectrum studied (Table 2; Figure 4) result in the onset and protracted development of the initial forearc basin that thickens at a decelerating rate of subsidence (Figure 9, left). The protracted growth of the initial forearc basin renders difficult the surface uplift of the forearc high, which cannot outpace subsidence (see video n2 in supplementary materials). Higher values of n_{μ} produce an early uplift at older times than our Base Model. The forearc high forms soon after the model onset, dividing an underdeveloped initial forearc basin. Uplift rates accelerate with time

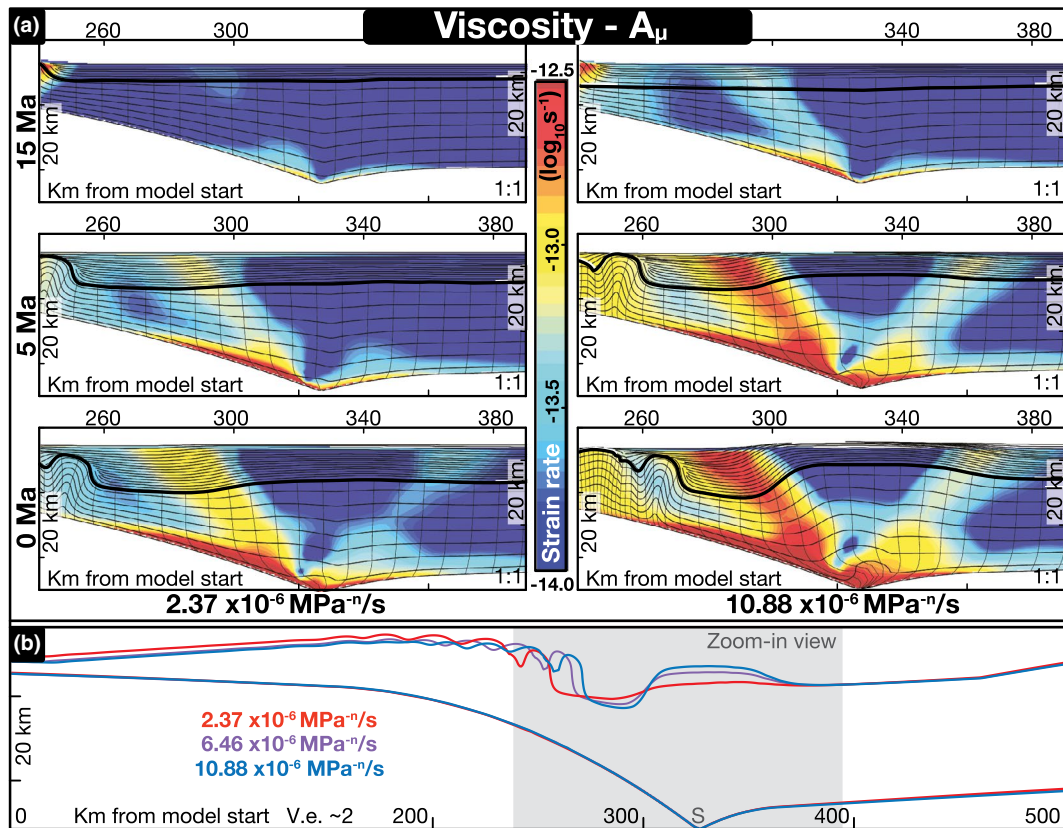


FIGURE 8 Variations in A_μ . Forearc high development with changes in the viscosity parameter A_μ . (a) Insets of the forearc high area for models with $A_\mu = 2.37 \times 10^{-6} \text{ MPa}^{-n}/\text{s}$ (left column) and $A_\mu = 10.88 \times 10^{-6} \text{ MPa}^{-n}/\text{s}$ (right column) at 15 Ma (top row), 5 Ma (middle row), and 0 Ma (bottom row). The individual black lines on top of the basement represent isochrones that reflect deformation since their successive inception in time, and thus the overall geometric relationships expected for strata. A thicker black line marks the basement-infill contact. (b) Line trace of the bottom of the crust and top of the basement in models with changes in the value of the viscosity parameter A_μ after a complete run. Vertical reference frame is taken from the 'S' point at the base of the crust. The dimmed grey box shows the approximate location of the zoom-in view in panel a. Upper panels are at 1:1 scale and the bottom panel is at 1:2 scale

in the forearc high and its width remains roughly constant (Figure 9, right). While the subsidence rates in the pro-wedge basin initially accelerate and then slow down at younger times, the retro-basin records the opposite trend in subsidence rates, with an older deceleration and a younger acceleration (Figure 9; video n6 in supplementary materials).

Within the parameter spectrum investigated (Table 2; Figure 4), the activation energy, Q , influences the occurrence and shape of uplift in the forearc high. Relatively low values result in a lower average effective viscosity that leads to an uplift that is larger and occurs at earlier stages than in our Base Model. Uplift of a convex up area blocks the development of the initial forearc basin, while inducing a second uplift in the model retro-wedge (Figure 10, left). Surface uplift in the forearc high outpaces the primary subsidence, and uplift rates accelerate with time. Subsidence rates in the forearc lows to the sides of the forearc high also accelerate with time (see video Q2 in supplementary materials). The width of the pro-basin decreases with time, while that of the retro-basin increases until it stabilises. Higher Q values accelerate the subsidence rates in the initial forearc basin, as the

basin becomes slightly narrower. Higher Q values effectively negate the thermal activation mechanism, thus viscosity remains low, and deformation under the forearc basin is almost fully inhibited (Figure 10, right). Even with an underfilled forearc basin, deformation never propagates landward of the active, critical wedge, and never approaches the S-point at the upper plate contact (Figure 10, right; video Q6 in supplementary materials).

5 | DISCUSSION

Models in this paper are based on the mechanism of forearc high uplift by deep crustal flow presented by Fuller et al. (2006), expanded and applied to the Anatolian margin by Fernández-Blanco et al. (2020). In these models, sediment accretion and syn-accretion sedimentation in the forearc basin lead to higher temperatures at deeper levels of orogenic wedges. Increased temperatures change the deformation mechanics in the lower crust from brittle to viscous. The thermal weakening of the lower crust

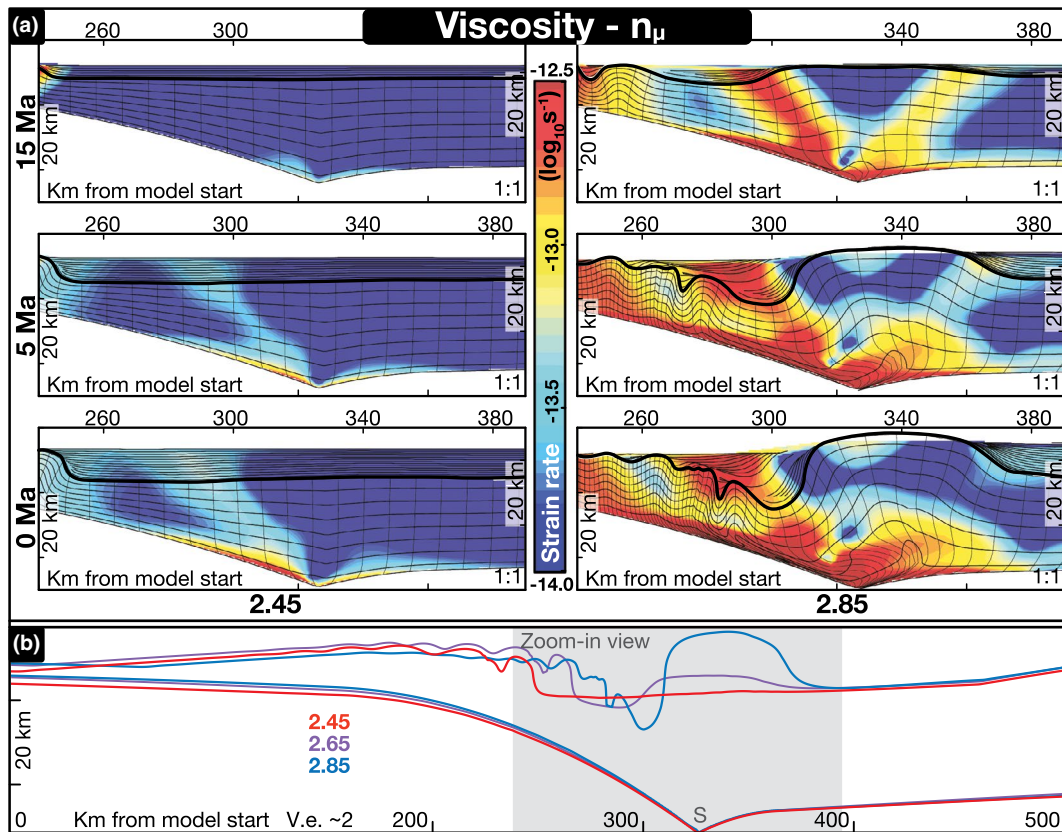


FIGURE 9 Variations in n_μ . Forearc high development with changes in the stress exponent of viscosity, n_μ . (a) Insets of the forearc high area for models with $n_\mu = 2.45$ (left column) and $n_\mu = 2.85$ (right column) at 15 Ma (top row), 5 Ma (middle row), and 0 Ma (bottom row). The individual black lines on top of the basement represent isochrones that reflect deformation since their successive inception in time, and thus the overall geometric relationships expected for strata. A thicker black line marks the basement-infill contact. (b) Line trace of the bottom of the crust and top of the basement in models with changes in the value of the viscosity parameter n_μ after a complete run. Vertical reference frame is taken from the 'S' point at the base of the crust. The dimmed grey box shows the approximate location of the zoom-in view in panel a. Upper panels are at 1:1 scale and the bottom panel is at 1:2 scale

results in ductile flow, and thickening and shortening of the wedge that leads to the dynamic growth of the forearc high through sustained accretionary growth. Models in this paper show how the sedimentation rate in the forearc basin, the rheological characteristics of the crust, and the initial thermal and viscous state of the wedge control the timing and geometry of early large-wavelength subsidence and subsequent short-wavelength uplift-subside of the forearc high-seaward basin pair.

5.1 | Thermo-viscous wedge geometry and forearc high growth

Subduction geometry and rheological parameters set the orogen cross-sectional shape and the non-linear growth of topography at the wedge rear. In the convergence direction and sense, the orogen has a critical, positive-alpha topography from trench to trench-slope break, a structural high at the trenchward edge of the forearc basin. Arcward of the trench-slope structural high, the wedge

is argued to be subcritical and the growing wedge taper is maintained by sedimentation rather than deformation (Fernández-Blanco et al., 2020; Fuller et al., 2006; Willett & Schlunegger, 2010). When the available accommodation space is filled with sediments, a wide negative-alpha basin develops that halts strain in the underlying wedge and sustains stable-wedge sliding above the decollement (Fuller et al., 2006; Willett & Schlunegger, 2010). In the negative-alpha basin, sediment thickness and thermal resistivity contribute to increased temperatures. Increased temperatures activate viscous flow in the lower crust leading to shortening, thickening, and uplift of a forearc high in the rear of the wedge, between the arc and the trench-slope forearc high, often directly within a pre-existing forearc basin (Fernández-Blanco et al., 2020). This thermo-viscous forearc high forms once temperatures increase to the point that viscous thickening occurs at significant rates under the regional compressive stresses.

The subsequent margin exhibits two structural forearc highs. The outer high at the trench-slope break bounds the forearc basin trenchward, and the second, inner high occurs

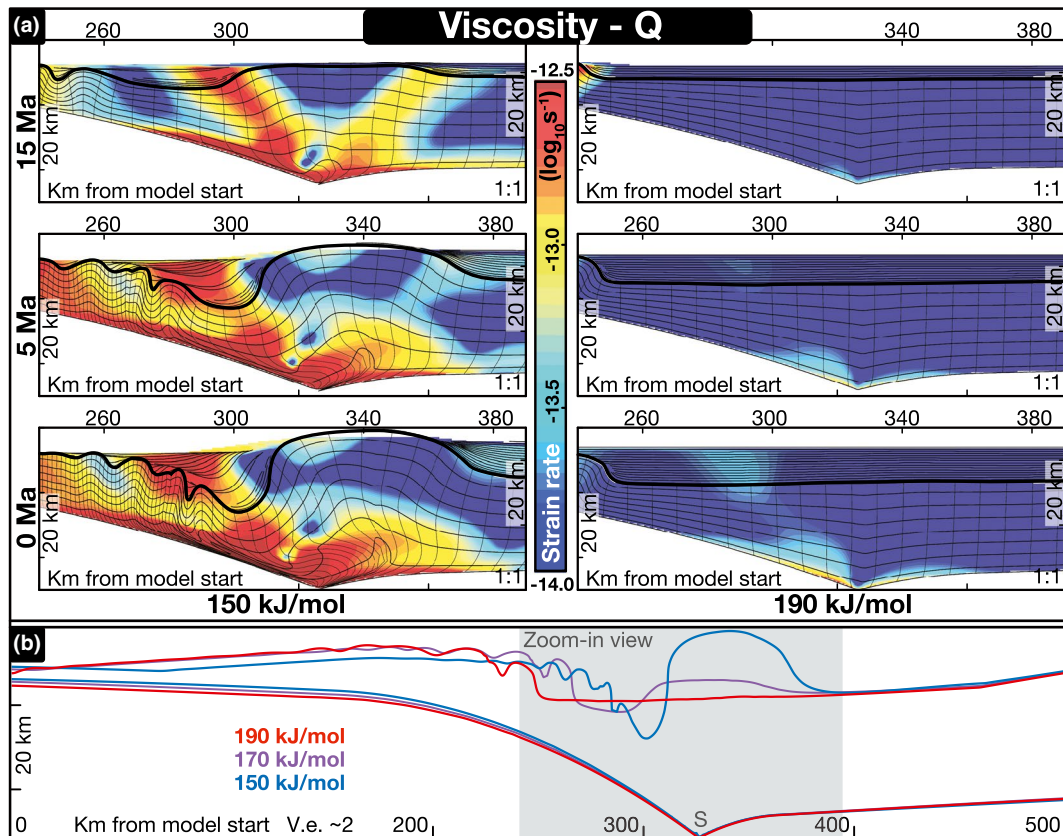


FIGURE 10 Variations in Q . Forearc high development with changes in the activation energy, Q . (a) Insets of the forearc high area for models with $Q = 150$ kJ/mol (left column) and $Q = 190$ kJ/mol (right column) at 15 Ma (top row), 5 Ma (middle row), and 0 Ma (bottom row). The individual black lines on top of the basement represent isochrones that reflect deformation since their successive deposition in time, and thus the overall geometric relationships expected for strata. A thicker black line marks the basement-infill contact. (b) Line trace of the bottom of the crust and top of the basement in models with changes in the value of the viscosity parameter Q after a complete run. Vertical reference frame is taken from the 'S' point at the base of the crust. The dimmed grey box shows the approximate location of the zoom-in view in panel a. Upper panels are at 1:1 scale and the bottom panel is at 1:2 scale

within or landward of the initial forearc basin. Our simulations suggest that the outer forearc high can grow without a material-strength backstop, solely as a function of the geometrical characteristics of the slab and wedge itself. The curvature of the subducting slab controls where sediment is detached from the oceanic plate and accreted into a critical wedge, and thus determines where and if the overriding wedge shifts from critical to stable. This transition between the critical, deforming wedge and the forearc basin where sedimentation stabilises the wedge, sets the location of the initial, outer forearc high. A late-stage, inner forearc high may initiate landward of this point in response to the thermal activation of crustal flow at the location where sediment blanketing leads to high temperature. This thermo-viscous forearc high is a consequence of more diffuse, viscous deformation within the region of highest temperature within the upper plate crust.

A particular set of mechanical conditions are required for this mechanism. First, the forearc must be under compression. Second, the initial forearc must be strong enough to support this compression without deformation, other than

accretion-driven wedge contraction. Finally, wedge thickening must be sufficient to heat the lower crust and decrease crustal viscosity to the point that deformation occurs at significant rates, leading to uplift in the forearc. Although these conditions are specific, our models show that they are well within the range of plausible; the uplift of the forearc high occurs for a wide range of values of thermal conductivity, viscosity, and sedimentation rate, and becomes more probable with time, as the forearc system enlarges and becomes more mature (Fernández-Blanco et al., 2020). The deep wedge thermal structure facilitates or hinders viscous deformation, and is of primary importance. If accretionary flux and convergence velocity are continuous and sufficient, a thermally activated viscosity drop at the base of the crust results in coupled, counteracting uplift and subsidence at the surface.

An implication of this model is that the forearc high uplift is not necessarily localised by a strong, deep backstop (e.g. Byrne et al., 1993), and its rather is keyed to the thermal structure of the forearc. In our models, the upper plate mantle is taken as non-deforming and thus serves as a type of backstop

where force balance requires a mechanical resistance to oppose the subducting plate. This resistance maintains the sense of compression across the domain but it does not localise deformation, despite the onset of viscous deformation near the S-point boundary. This is largely coincidental, for the highest temperatures and the lowest viscosities are located near the S-point, and given that temperature and its changes are the necessary condition for the resulting temporal evolution of deformation and forearc uplift. In this sense, the thermo-viscous forearc high can be regarded as an integral part of an accretionary wedge that develops at an advanced stage of wedge growth (e.g. Pavlis & Bruhn, 1983) as a function of the accretionary flux, wedge viscosity, and synorogenic sedimentation.

5.2 | Synorogenic sedimentation controls on forearc high growth

Variations in the sedimentation rate significantly influence the growth of the margin (Figure 7). Synorogenic sedimentation and growth of the main forearc basin increase the temperature of the lower crust through the thermal resistance of the sedimentary pile. The increased thickness of the overburden increases the temperature of the underlying crust, and if the sediments have low thermal conductivity, this 'thermal blanketing' effect becomes more prominent. The effect is transient; while the low temperature of basinal sediments tends to lower the geothermal gradient, the gradient is eventually restored by diffusive heating in the basin, which results in high temperatures in the lower crust.

Sedimentation and deformational crustal thickening both contribute to the progressive thermal activation of ductile strain in the lower crust and ultimately propel the growth of a forearc high. When sediment input is small, there is no sediment loading of the critical accretionary wedge and the resultant deformation leads to the development of structural highs along the margin. A broad forearc high develops with small flanking basins (Figure 7, left). As sedimentation increases, long-wavelength subsidence takes place at model initial stages and the onset of the forearc high growth is delayed (Figure 7, right). Models with higher maximum sedimentation rate have a larger sediment load and thus suppress the deformational growth of a forearc high, and retain protracted long-wavelength subsidence.

Our models of accretionary margins show that if the amount of incoming sediments at the trench remains constant, variations in the sedimentation rate control the growth rate and thus the occurrence of surface uplift in the forearc high regions. With a high sediment flux and large accommodation space, the mass flux by sediment deposition can be the largest flux in the system. These results lead to the counterintuitive postulation that regional subsidence in the forearc basin can be the main cause behind surface uplift in a new forearc high internal to the basin.

5.3 | Wedge rheology controls on forearc high growth

Variations in initial wedge viscosity markedly influence the growth of the margin (Figures 8 to 10). Wedge viscosity and its thermally-controlled dynamic state lead to different degrees of strain localisation that in turn control the occurrence, age, wavelength, and rate of uplift in the wedge. Higher initial wedge viscosities, achieved through some combination of low A_{μ} , low n_{μ} , and/or high Q , limit the viscous flow, delaying or preventing the uplift of the forearc high, and lead to stable wedges that widen and thicken only by sedimentation and subsidence in the forearc. In contrast, under the same accretionary flux, lower initial wedge viscosities, achieved through some combination of high A_{μ} , high n_{μ} , and/or low Q , facilitate ductile flow and the uplift of the forearc high by shortening and thickening. We thus infer that low viscosity at initial stages of wedge growth has similar effects as high temperatures in the evolution of the internal sectors of the wedge, and both parameters act to accelerate the morphologic evolution of mature wedges.

As suggested by previous studies (Vanderhaeghe et al., 2003), lowering the initial viscosity of the wedge results in larger decoupling of the lower crust, and increasing the extent of the viscous flow landwards. Our models further suggest that this effect is to a large extent controlled by syn-accretion sedimentation. Lower initial wedge viscosity results in a broader and more pronounced forearc high, sharply bounded by a seaward and a landward basin that continue to subside by the sedimentary load. Sedimentation in these bounding forearc lows controls the extent of viscous flow and thus that of the uplift in the forearc high. Accommodation space in the negative-alpha basin at the front of the forearc high is controlled by the high in its proximal basin edge and by tectonic uplift of the slope-trench break in its distal basin edge (Willett & Schlunegger, 2010). In contrast, accommodation space in the forearc basin at the back of the forearc high is solely controlled by the forearc high. As a result, accommodation space increases at a faster pace in the seaward basin, in turn leading to an extra sedimentary load that translates the viscous flow of the lower crust farther landward. This effect, facilitated by lower viscosity and larger decoupling of the negative-alpha region, increases the volume of viscously deforming rock in the lower crust and leads to lateral growth of the forearc high into a plateau.

5.4 | Coupled control of sedimentation and viscosity on forearc high growth

The interplay between sedimentation and viscosity is illustrated by the range of models presented in this paper and summarised in Figure 11. Although specific rheological parameters affect deformation differently, the first-order effect of rheology can be expressed through an average effective

viscosity of the lowermost crust of the upper plate, where deformation through thermal activation initiates (Fernández-Blanco et al., 2020). Models in Figure 11 show the influence of viscosity on structural style, from early, intense crustal thickening and forearc uplift with a localised forearc basin (Figure 11, lower left) to a broad basin blanketing both upper plate, slab, and the interface, without deformation in the lower crust (Figure 11, upper right). In this latter example, the material is too strong or too cold to sustain deformation, despite the thermal effects of sediment deposition. The end result is a wide, negative-alpha basin with no mechanical backstop supporting the critical wedge (Figure 11, upper right). In the opposite extreme (Figure 11, lower left), the crust is very weak, deformation is extensive throughout the forearc, and basins are small and structurally controlled. The accretionary wedge backthrusts over the upper plate upper mantle, which subsequently acts as a low-angle mechanical backstop.

The sedimentation effect is more subtle as it depends on the interplay with the rheology (Figure 11, upper left to lower right diagonal). For most of the rheology models considered in this contribution, high sedimentation leads to thermal weakening and broad zones of deformation (Figure 11, lower right). Low sedimentation produces a smaller loading effect on the critical wedge that leads to brittle-dominated deformation that spans a broader zone, even in the absence of thermally-activated viscous deformation (Figure 11, upper left). Between end-member models, when sedimentation is sufficient to suppress brittle deformation and insufficient to increase temperatures, minimal deformation results in models that appear much like the strong rheology case, shown in the upper right.

Forearc high growth thus interacts with sedimentation through two competing processes. First, sedimentation provides a mechanical load to the accretionary wedge, determining whether the wedge deforms critically, and uplifts the forearc high, or is held in a sustained sub-critical or stable state with no internal deformation. Second, the sediments deposited in a wedge-top or forearc basin act as a thermal insulator that heats the underlying crust and eventually leads to thermal weakening, thereby increasing deformation, including uplift. Therefore, sedimentation can either suppress deformation (loading) or increase deformation (heating). It is thus not surprising that the response to sedimentation is highly complex and nonlinear, and that a varied set of structures and basin architectures develop depending on the interplay between deformation and sedimentation (Figure 11).

5.5 | The Anatolian margin and the forearc high uplift in South Turkey

The analysis of the structures observed along the regional 2D geologic transect of the central Cyprus arc suggests shortening

from the trench to south Turkey (Figure 3). The type, distribution, relative age, and geometry of these contractional structures are compatible with their development in relation to a wide accretionary subduction system (e.g. Dickinson & Seely, 1979) (Figure 1). Our simulations can reproduce the overall geometry and the main contact relationships as well as the main vertical tectonic events of the south Anatolian upper plate and are also consistent with other geologic observations. These include early continuity and later disruption of Miocene basins in the presence of brittle, regional-scale accommodating structures in the seaward regions, that is, the trench, the trench-slope, and the trench-slope break areas, and broad monoclinial flexure above ductile strain in the otherwise largely undeformed landward forearc basin region (Figures 1, 3 and 5) (Fernández-Blanco et al., 2020). Therefore, mechanical accretion from Cyprus dominates deformation in the Mesaoria Basin and the Kyrenia Range, in Central Cyprus, while ductile deformation at deeper levels controls the growth of the Central Taurus Mountains, in south Turkey, and thus the evolution of the basins of Cilicia and Mut (Figures 1 and 12).

South Turkey surface uplift and growth of the modern Central Taurus Mountains since ~ 8 Ma (e.g. Cosentino et al., 2012; Meijers et al., 2018) and concomitant offshore subsidence (Walsh-Kennedy et al., 2014) developed the monoclinial flexure of Miocene rocks (Fernández-Blanco et al., 2019) as it divided the forearc basin into the landward uplifted Mut Basin, and the seaward subsided Cilicia Basin. Such coupled, short-wavelength vertical motions can be explained by the mechanism for thermo-viscous forearc high formation during the accretionary evolution of the south Anatolian margin along Central Cyprus (Figures 5 and 12). The wavelength of uplift in the Central Taurus Mountains (Fernández-Blanco et al., 2019; Walsh-Kennedy et al., 2014) and the presence of the Cyprus slab under the range (e.g. Abgarmi et al., 2017; Bakırcı et al., 2012) agree well with thermo-viscous forearc models but is inconsistent with models involving slab break-off (e.g. Schildgen et al., 2014). The location of maximum uplift above the area of maximum thickness in the Anatolian crust (Figure 3), the absence of accommodation structures along the uplifted area (Fernández-Blanco et al., 2019), and the low seismicity along the margin (Imprescia et al., 2012) are other observations compatible with broad upwarping due to deep crustal thickening beneath the modern Central Taurus Mountains.

The south Anatolian margin has a few unique characteristics that differentiate it from other accretionary margins worldwide. Arguably, foremost is the presence of the Troodos Ophiolite, emplaced within the forearc region. Its emplacement predates the tectonic events of this paper, but it could affect the mechanics of the wedge given its high strength relative to accreted sediments. Its position in the forearc is nevertheless primarily in the undeforming, 'stable' section of

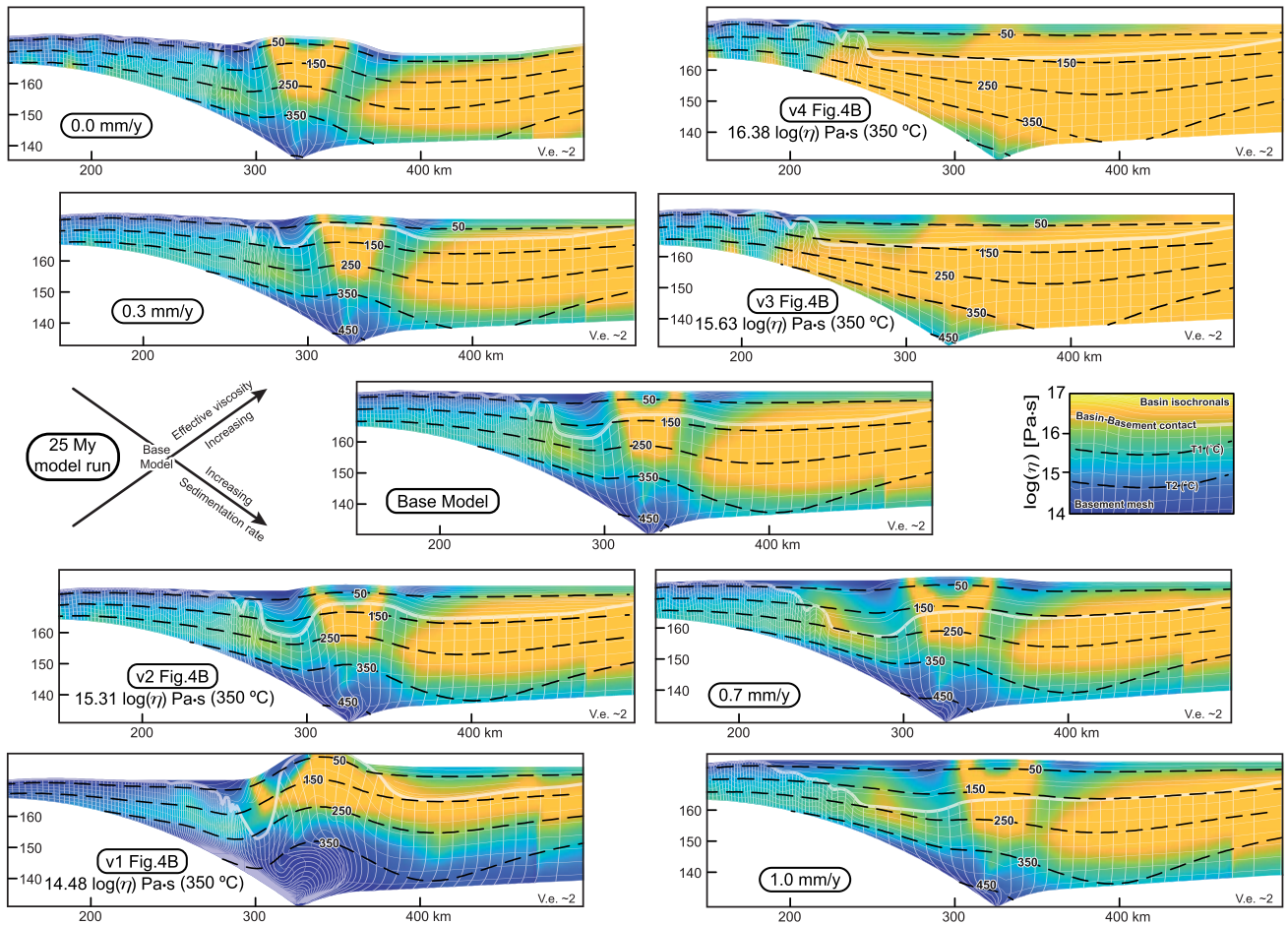


FIGURE 11 Sedimentation rate and viscosity controls on wedge and basin morphology. Changes in wedge morphology and basin architecture as a function of maximum sedimentation rate and crustal viscosity shown along two axes that cross on the Base Model. The top-left to bottom-right diagonal shows models with varying sedimentation rates between 0 mm/year in the top-left and 10 mm/year in the bottom-right, with a fixed rheology model (Base Model -Figure 4). The bottom-left to top-right diagonal shows models as a function of rheology, parameterised by effective log viscosity at 350°C and strain rate of 10–14 of 14.48 Pa-s in bottom-left to 16.38 Pa-s in the top-right. Effective viscosity models, V1 to V5, are shown in Figure 4b. Light white lines show the deformation mesh of the mechanical model. A grid represents the basement and originally-horizontal lines are isochrones for the sedimentary cover, and their contact (top of the basement), is shown with thicker stroke. Isotherms are in dashed black lines, with numbers in °C. Figure shows the model sectors with morphological variations, between 150 km and 500 km, and excludes far sides, where wedge morphology is similar

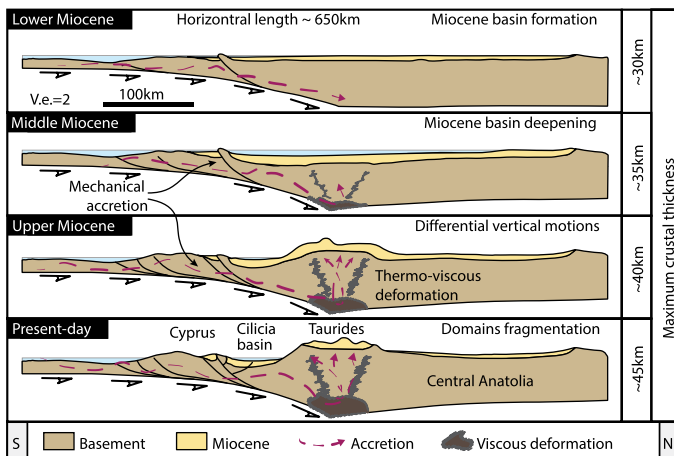


FIGURE 12 Conceptual evolution of the Anatolian margin in Central Cyprus

the wedge, so it seems not to have affected tectonic processes trenchward or arcward.

Although every accretionary margin has its unique characteristics based on accretion history, volcanism, thermal conditions of the slab, and other variables, commonalities also exist. The thermo-viscous forearc high uplift presented here provides an explanation for the growth of broad, anomalously uplifted hinterland areas in other accretionary margins. These include the Kodiak and Eastern Aleutian islands, in the Alaskan margin; the Olympic Mts, in the Cascadia margin; the Nankai margin, and the Makran region, in southern Iran. These margins are mature and have arc-trench gaps of ~300 km, with large accretionary wedges and wedge-top basins, and forearc highs at >50 km of the trench-slope break. All these margins are also consistent with the principle characteristic of the viscous forearc model, a transient evolution, with a long history of sedimentation across a forearc, and the compartmentalisation of deformation between basins and structural highs.

6 | CONCLUSION

Our integration and interpretation of data in a transect along the Central Cyprus subduction suggest its evolution by subduction accretion since the Early Miocene. Simulations with 2D thermo-mechanical finite elements of accreting subduction wedges aimed at reproducing the first-order geology and vertical tectonic motions along the transect show that; (a) frictional-mechanical deformation driven by sediment accretion sets the time sequence of structures and the topobathymetry in the trench, trench slope, and seaward areas of the forearc, and (b) viscous-thermal deformation dominates in landward areas of the forearc and controls forearc high growth and its shape.

The resultant geometry of our models includes closed wedge-top basins, including a large forearc basin that is later disrupted by the forearc high. Sedimentary filling of the wedge-top basins determines if, and how fast the accretionary wedge grows landward, and the growth by the deformation of an initial, brittle forearc high above a curved slab, with no need for a mechanical backstop. Sedimentation in the forearc basin results in the heating of the crust underneath, and if continued, a thermally-induced viscosity drop in the lower crust leads to weakening and ductile flow resulting in the uplift of a new forearc high, driven by ductile deformation. The occurrence, geometry, and timing of vertical motions along the accretionary margin and in the forearc high vary in relation to sediment availability, deposition rates, and viscosity, through its dependence on temperature. While low sedimentation rates lead to thin forearc basins and results in forearc high uplifting at earlier times of margin accretion, progressively

higher sedimentation rates result in more pronounced basin thickening, delaying surface uplift through brittle growth mechanisms. Similarly, lower viscosities produce prominent rounded-shaped forearc highs developing at earlier model run times, while increasing viscosities result in the uplift of an area that develops at progressively younger times and has an increasingly flatter and broader top surface. Very large sedimentation rates and/or higher viscosities stabilise the accretionary wedge and halt forearc high growth.

Models corroborate that ductile deformation, lead by thermally-activated viscosity at the base of the Anatolian crust and yielded by the accretion of sediments incoming in the Cyprus Arc, is a viable mechanism driving the surface uplift that raised the modern Central Taurus Mountains. Our simulations reproduce upper plate deformation structures and modern sedimentary architectures along Central Cyprus and can be extrapolated to other accretionary margins with similar morphologies and vertical motions in time.

ACKNOWLEDGEMENTS

We are very thankful for the critical, the collegial reviews of Terry Pavlis and John P. Platt that help strengthen the final manuscript, and editorial handling of Craig Magee. We thank the Nederlandse Organisatie voor Wetenschappelijk Onderzoek (NWO) for founding this study as a part of the Vertical Anatolian Movement Project (VAMP) - Miocene tectonics in the Central Anatolia Plateau (855.01.142 (07-TOPO-EUROPE-FP-013)) a European Science Foundation (ESF) EuroCORE project within TOPOEurope.

CONFLICTS OF INTEREST

The authors declare that they have no known competing financial interests or personal relationships that could have appeared to influence the work reported in this paper.

PEER REVIEW

The peer review history for this article is available at <https://publons.com/publon/10.1111/bre.12518>.

DATA AVAILABILITY STATEMENT

The data that support the findings of this study are available from the corresponding author upon reasonable request.

ORCID

David Fernández-Blanco  <https://orcid.org/0000-0002-5326-9164>

Utsav Mannu  <https://orcid.org/0000-0003-2416-3958>

REFERENCES

- Abgarmi, B., Delph, J. R., Arda Ozacar, A., Beck, S. L., Zandt, G., Sandvol, E., Turkelli, N., & Berk Biryol, C. (2017). Structure of the crust and African slab beneath the central Anatolian plateau from

- receiver functions: New insights on isostatic compensation and slab dynamics. *Geosphere*, 13, 1774–1787. <https://doi.org/10.1130/GES01509.1>
- Aksu, A. E., Calon, T. J., Hall, J., Mansfield, S., & Yaşar, D. (2005). The Cilicia-Adana basin complex, Eastern Mediterranean: Neogene evolution of an active fore-arc basin in an obliquely convergent margin. *Marine Geology*, 221, 121–159. <https://doi.org/10.1016/j.margeo.2005.03.011>
- Ates, A., Kearey, P., & Tufan, S. (1999). New gravity and magnetic anomaly maps of Turkey. *Geophysical Journal International*, 136(2), 499–502.
- Bakırcı, T., Yoshizawa, K., & Özer, M. (2012). Three-dimensional S-wave structure of the upper mantle beneath Turkey from surface wave tomography. *Geophysical Journal International*, 190, 1058–1076. <https://doi.org/10.1111/j.1365-246X.2012.05526.x>
- Biryol, C., Beck, S. L., Zandt, G., & Özacar, A. (2011). Segmented African lithosphere beneath the Anatolian region inferred from teleseismic P-wave tomography. *Geophysical Journal International*, 184, 1037–1057. <https://doi.org/10.1111/j.1365-246X.2010.04910.x>
- Byrne, D. E., Wang, W.-H., & Davis, D. M. (1993). Mechanical role of backstops in the growth of forearcs. *Tectonics*, 12, 123–144. <https://doi.org/10.1029/92TC00618>
- Calon, T. J., Aksu, A. E., & Hall, J. (2005a). The Neogene evolution of the Outer Latakia Basin and its extension into the Eastern Mesaoria Basin (Cyprus), Eastern Mediterranean. *Marine Geology*, 221, 61–94. <https://doi.org/10.1016/j.margeo.2005.03.013>
- Calon, T. J., Aksu, A. E., & Hall, J. (2005b). The Oligocene-Recent evolution of the Mesaoria Basin (Cyprus) and its western marine extension, Eastern Mediterranean. *Marine Geology*, 221, 95–120. <https://doi.org/10.1016/j.margeo.2005.03.012>
- Cassola, T. (2013). Mechanics of forearc basins, Ph.D. Thesis. ETH Zurich.
- Christensen, N. I., & Mooney, W. D. (1995). Seismic velocity structure and composition of the continental crust: A global view. *Journal of Geophysical Research*, 100, 9761–9788. <https://doi.org/10.1029/95JB00259>
- Çiner, A., Karabiyikoğlu, M., Monod, O., Deynoux, M., & Tuzcu, S. (2008). Late Cenozoic sedimentary evolution of the Antalya Basin, Southern Turkey. *Turkish Journal of Earth Sciences*, 17, 1–41.
- Cosentino, D., Schildgen, T., Cipollari, P., Faranda, C., Gliozzi, E., Hudáčková, N., Lucifora, S., & Strecker, M. R. (2012). Late Miocene surface uplift of the southern margin of the Central Anatolian Plateau, Central Taurides, Turkey. *GSA Bulletin*, 124, 133–145. <https://doi.org/10.1130/B30466.1>
- Dahlen, F. A. (1984). Noncohesive critical Coulomb wedges: An exact solution. *Journal of Geophysical Research*, 89, 10125–10133. <https://doi.org/10.1029/JB089iB12p10125>
- Davis, D., Suppe, J., & Dahlen, F. A. (1983). Mechanics of fold-and-thrust belts and accretionary wedges. *Journal of Geophysical Research*. <https://doi.org/10.1029/JB088iB02p01153>
- DeCelles, P. G., & Giles, K. A. (1996). Foreland basin systems. *Basin Research*, 8, 105–123. <https://doi.org/10.1046/j.1365-2117.1996.01491.x>
- Delph, J. R., Abgarmi, B., Ward, K. M., Beck, S. L., Arda Özacar, A., Zandt, G., Sandvol, E., Türkelli, N., & Kalafat, D. (2017). The effects of subduction termination on the continental lithosphere: Linking volcanism, deformation, surface uplift, and slab tearing in central Anatolia. *Geosphere*, 13, 1788–1805. <https://doi.org/10.1130/GES01478.1>
- Dickinson, W. R., & Seely, D. R. (1979). Structure and stratigraphy of forearc regions. *AAPG Bulletin*, 63, 2–31.
- Dziewonski, A. M., & Anderson, D. L. (1981). Preliminary reference Earth model. *Physics of the Earth and Planetary Interiors*, 25, 297–356. [https://doi.org/10.1016/0031-9201\(81\)90046-7](https://doi.org/10.1016/0031-9201(81)90046-7)
- Erdős, Z., Huismans, R. S., & van der Beek, P. (2015). First-order control of syntectonic sedimentation on crustal-scale structure of mountain belts. *Journal of Geophysical Research*, [solid Earth], 120, 5362–5377. <https://doi.org/10.1002/2014JB011785>
- Ergün, M., Okay, S., Sari, C., Zafer Oral, E., Ash, M., Hall, J., & Miller, H. (2005). Gravity anomalies of the Cyprus Arc and their tectonic implications. *Marine Geology*, 221, 349–358. <https://doi.org/10.1016/j.margeo.2005.03.004>
- Fernández-Blanco, D. (2014). Evolution of Orogenic Plateaus at Subduction Zones: Sinking and raising the southern margin of the Central Anatolian Plateau. Ph.D. Thesis. Vrije Universiteit Amsterdam.
- Fernández-Blanco, D., Bertotti, G., Aksu, A., & Hall, J. (2019). Monoclinical flexure of orogenic plateau margins during subduction, as recorded in south Turkey. *Basin Research*, 31(4), 709–727. <https://doi.org/10.1111/bre.12341>
- Fernández-Blanco, D., Bertotti, G., & Çiner, A. (2013). Cenozoic tectonics of the Tuz Gölü Basin (Central Anatolia Plateau, Turkey). *Turkish Journal of Earth Sciences*, 22, 715–738. <https://doi.org/10.3906/yer-1206-7>
- Fernández-Blanco, D., Mannu, U., Bertotti, G., & Willett, S. D. (2020). Forearc high uplift by lower crustal flow during growth of the Cyprus-Anatolian margin. *Earth and Planetary Science Letters*, 544, 116314. <https://doi.org/10.1016/j.epsl.2020.116314>
- Fillon, C., Huismans, R. S., & van der Beek, P. (2013). Syntectonic sedimentation effects on the growth of fold-and-thrust belts. *Geology*, 41, 83–86. <https://doi.org/10.1130/G33531.1>
- Flemings, P. B., & Saffer, D. M. (2018). Pressure and stress prediction in the Nankai accretionary prism: A critical state soil mechanics porosity-based approach. *Journal of Geophysical Research: Solid Earth*, 123, 1089–1115.
- Fuller, C. W. (2006). Controls on the structural morphology and subduction-thrust seismicity of accretionary margins, Ph.D. Thesis. University of Washington.
- Fuller, C. W., Willett, S. D., & Brandon, M. T. (2006). Formation of forearc basins and their influence on subduction zone earthquakes. *Geology*, 34, 65–68. <https://doi.org/10.1130/G21828.1>
- Fuller, C. W., Willett, S. D., Fisher, D., & Lu, C. Y. (2006). A thermomechanical wedge model of Taiwan constrained by fission-track thermochronometry. *Tectonophysics*, 425, 1–24. <https://doi.org/10.1016/j.tecto.2006.05.018>
- Fullsack, P. (1995). An arbitrary Lagrangian-Eulerian formulation for creeping flows and its application in tectonic models. *Geophysical Journal International*, 120, 1–23. <https://doi.org/10.1111/j.1365-246X.1995.tb05908.x>
- Harrison, R. W., Newell, W. L., Bathanlı, H., Panayides, I., McGeehin, J. P., Mahan, S. A., Özhür, A., Tsiolkakis, E., & Necdet, M. (2004). Tectonic framework and Late Cenozoic tectonic history of the northern part of Cyprus: Implications for earthquake hazards and regional tectonics. *Journal of Asian Earth Sciences*, 23, 191–210. [https://doi.org/10.1016/S1367-9120\(03\)00095-6](https://doi.org/10.1016/S1367-9120(03)00095-6)
- Hofmeister, A. M. (1999). Mantle values of thermal conductivity and the geotherm from phonon lifetimes. *Science*, 283, 1699–1706. <https://doi.org/10.1126/science.283.5408.1699>
- Ikari, M. J., & Kopf, A. J. (2011). Cohesive strength of clay-rich sediment. *Geophysical Research Letters*, 38(16).

- Imprescia, P., Pondrelli, S., Vannucci, G., & Gresta, S. (2012). Regional centroid moment tensor solutions in Cyprus from 1977 to the present and seismotectonic implications. *Journal of Seismology*, *16*, 147–167. <https://doi.org/10.1007/s10950-011-9254-7>
- Jaupart, C., & Mareschal, J. C. (2005). Production from Heat Flow Data. *The Crust*, *3*, 65–84.
- Karig, D. E., & SHARMAN III, G. F. (1975). Subduction and accretion in trenches. *Geological Society of America Bulletin*, *86*(3), 377–389. [http://dx.doi.org/10.1130/0016-7606\(1975\)86<377:SAAIT>2.0.CO;2](http://dx.doi.org/10.1130/0016-7606(1975)86<377:SAAIT>2.0.CO;2)
- Koons, P. O. (1990). Two-sided orogen: Collision and erosion from the sandbox to the Southern Alps, New Zealand. *Geology*, *18*, 679–682. [https://doi.org/10.1130/0091-7613\(1990\)018<0679:TSOCAE>2.3.CO;2](https://doi.org/10.1130/0091-7613(1990)018<0679:TSOCAE>2.3.CO;2)
- Kopp, H., & Kukowski, N. (2003). Backstop geometry and accretionary mechanics of the Sunda margin. *Tectonics*, *22*(6). <https://doi.org/10.1029/2002TC001420>
- Koulakov, I., & Sobolev, S. V. (2006). Moho depth and three-dimensional P and S structure of the crust and uppermost mantle in the Eastern Mediterranean and Middle East derived from tomographic inversion of local ISC data. *Geophysical Journal International*, *164*, 218–235.
- Makris, J., & Stobbe, C. (1984). Physical properties and state of the crust and upper mantle of the Eastern Mediterranean Sea deduced from geophysical data. *Marine Geology*, *55*, 347–363. [https://doi.org/10.1016/0025-3227\(84\)90076-8](https://doi.org/10.1016/0025-3227(84)90076-8)
- Mart, Y., & Ryan, W. B. (2002). The complex tectonic regime of Cyprus arc: a short review. *Israel Journal of Earth Sciences*, *51*, 117–134.
- McCay, G. (2010). Tectonic-sedimentary evolution of the Girne (Kyrenia) Range and the Mesarya (Mesaoria) Basin, North Cyprus. Ph.D. University of Edinburgh.
- McCay, G. A., & Robertson, A. (2013). Upper Miocene-Pleistocene deformation of the Girne (Kyrenia) Range and Dar Dere (Ovgos) lineaments, northern Cyprus: Role in collision and tectonic escape in the easternmost Mediterranean region. *Geological Society, London, Special Publications*, *371*(1), 421–445
- Meijers, M. J. M., Brocard, G. Y., Cosca, M. A., Lüdecke, T., Teyssier, C., Whitney, D. L., & Mulch, A. (2018). Rapid late Miocene surface uplift of the Central Anatolian Plateau margin. *Earth and Planetary Science Letters*, *497*, 29–41. <https://doi.org/10.1016/j.epsl.2018.05.040>
- Mutlu, A., & Karabulut, H. (2011). Anisotropic Pn tomography of Turkey and adjacent regions. *Geophysical Journal International*, *187*, 1743–1758. <https://doi.org/10.1111/j.1365-246X.2011.05235.x>
- Nayar, K. G., Sharqawy, M. H., Banchik, L. D., Lienhard V, J. H. (2016). Thermophysical properties of seawater: A review and new correlations that include pressure dependence. *Desalination*, *390*, 1–24. <https://doi.org/10.1016/j.desal.2016.02.024>
- Özener, M. S., & Holt, W. E. (2010). The dynamics of the eastern Mediterranean and eastern Turkey. *Geophysical Journal International*, *183*, 1165–1184. <https://doi.org/10.1111/j.1365-246X.2010.04819.x>
- Pasyanos, M. E. (2010). Lithospheric thickness modeled from long-period surface wave dispersion. *Tectonophysics*, *481*, 38–50. <https://doi.org/10.1016/j.tecto.2009.02.023>
- Pavlis, T. L., & Bruhn, R. L. (1983). Deep-seated flow as a mechanism for the uplift of broad forearc ridges and its role in the exposure of high P/T metamorphic terranes. *Tectonics*, *2*, 473–497. <https://doi.org/10.1029/TC002i005p00473>
- Platt, J. P. (1986). Dynamics of orogenic wedges and the uplift of high-pressure metamorphic rocks. *GSA Bulletin*, *97*, 1037–1053. [https://doi.org/10.1130/0016-7606\(1986\)97<1037:DOOWA T>2.0.CO;2](https://doi.org/10.1130/0016-7606(1986)97<1037:DOOWA T>2.0.CO;2)
- Pope, D. C., & Willett, S. D. (1998). Thermal-mechanical model for crustal thickening in the central Andes driven by ablative subduction. *Geology*, *26*, 511–514. [https://doi.org/10.1130/0091-7613\(1998\)026<0511:TMMFCT>2.3.CO;2](https://doi.org/10.1130/0091-7613(1998)026<0511:TMMFCT>2.3.CO;2)
- Ranalli, G. (1995). *Rheology of the earth*. Springer Science & Business Media.
- Reilinger, R., McClusky, S., Vernant, P., Lawrence, S., Ergintav, S., Cakmak, R., Ozener, H., Kadirov, F., Guliev, I., Stepanyan, R., Nadariya, M., Hahubia, G., Mahmoud, S., Sakr, K., ArRajehi, A., Paradissis, D., Al-Aydrus, A., Prilepin, M., Guseva, T., ... Karam, G. (2006). GPS constraints on continental deformation in the Africa-Arabia-Eurasia continental collision zone and implications for the dynamics of plate interactions: Eastern Mediterranean active tectonics. *Journal of Geophysical Research*, *111*(B5). <https://doi.org/10.1029/2005JB004051>
- Robertson, A. H. (1998a). Mesozoic-Tertiary tectonic evolution of the easternmost Mediterranean area: integration of marine and land evidence. *Proceedings of the Ocean Drilling Program, Scientific results*, Vol. 160; Chapter 54.
- Robertson, A. H. F. (1998b). Tectonic significance of the Eratosthenes Seamount: A continental fragment in the process of collision with a subduction zone in the eastern Mediterranean (Ocean Drilling Program Leg 160). *Tectonophysics*, *298*, 63–82. [https://doi.org/10.1016/S0040-1951\(98\)00178-4](https://doi.org/10.1016/S0040-1951(98)00178-4)
- Schildgen, T. F., Yildirim, C., Cosentino, D., & Strecker, M. R. (2014). Linking slab break-off, Hellenic trench retreat, and uplift of the Central and Eastern Anatolian plateaus. *Earth-Science Reviews*, *128*, 147–168. <https://doi.org/10.1016/j.earscirev.2013.11.006>
- Smit, J. H. W., Brun, J. P., & Sokoutis, D. (2003). Deformation of brittle-ductile thrust wedges in experiments and nature. *Journal of Geophysical Research*, *108*, 3. <https://doi.org/10.1029/2002JB002190>
- Stephenson, R. A., Mart, Y., Okay, A., Robertson, A., Saintot, A., Stovba, S., & Khriachtchevskaia, O. (2004). TRANSMED Transect VIII: Eastern European Craton to Arabian Craton (Red Star to Red Sea). In *The TRANSMED Atlas: The Mediterranean region from crust to mantle*. (pp. 120–127).
- Turcotte, D. L., & Schubert, G. (2002). *Geodynamics*. Cambridge university press.
- Vanderhaeghe, O., Medvedev, S., Fullsack, P., Beaumont, C., & Jamieson, R. A. (2003). Evolution of orogenic wedges and continental plateaus: Insights from crustal thermal-mechanical models overlying subducting mantle lithosphere. *Geophysical Journal International*, *153*, 27–51. <https://doi.org/10.1046/j.1365-246X.2003.01861.x>
- Walsh-Kennedy, S., Aksu, A. E., Hall, J., Hiscott, R. N., Yaltrak, C., & Çifçi, G. (2014). Source to sink: The development of the latest Messinian to Pliocene-Quaternary Cilicia and Adana Basins and their linkages with the onland Mut Basin, eastern Mediterranean. *Tectonophysics*, *622*, 1–21. <https://doi.org/10.1016/j.tecto.2014.01.019>
- Willett, S. D. (1992). Dynamic and kinematic growth and change of a Coulomb wedge. In K. R. McClay (Ed.), *Thrust tectonics* (pp. 19–31). Springer.
- Willett, S. D. (1999). Orogeny and orography: The effects of erosion on the structure of mountain belts. *Journal of Geophysical Research*, *104*, 28957–28981. <https://doi.org/10.1029/1999JB900248>

Willett, S.D., & Schlunegger, F. (2010). The last phase of deposition in the Swiss Molasse Basin: From foredeep to negative-alpha basin. *Basin Research*, 22, 623–639. <https://doi.org/10.1111/j.1365-2117.2009.00435.x>

SUPPORTING INFORMATION

Additional supporting information may be found online in the Supporting Information section.

How to cite this article: Fernández-Blanco D, Mannu U, Cassola T, Bertotti G, Willett SD. Sedimentation and viscosity controls on forearc high growth. *Basin Res.* 2021;33:1384–1406. <https://doi.org/10.1111/bre.12518>